C. R. Physique 19 (2018) 688–709

Contents lists available at ScienceDirect

Comptes Rendus Physique

www.sciencedirect.com

New trends in metallic alloys / Alliages métalliques : nouvelles tendances

Recent advances in the metallurgy of aluminum alloys. Part II: Age hardening

Développements récents en métallurgie des alliages d'aluminium. Deuxième partie : durcissement par revenu

Christophe Sigli [a], Frédéric De Geuser [b], Alexis Deschamps [b], Joël Lépinoux [b], Michel Perez [c]

[a] *Constellium Technology Center, CS 10027, 38341 Voreppe Cedex, France*
[b] *Université Grenoble Alpes, CNRS, Grenoble INP, SIMAP, 38000 Grenoble, France*
[c] *Université de Lyon, INSA Lyon, MATEIS – UMR CNRS 5510, bâtiment Saint-Exupéry, 25, avenue Jean-Capelle, 69621 Villeurbanne cedex, France*

ARTICLE INFO

Article history:
Available online 9 November 2018

Keywords:
Age hardening
Strengthening
Guinier–Prestone
Monte Carlo
Nucleation
Coarsening

Mots-clés :
Revenu
Durcissement
Guinier–Preston
Monte Carlo
Germination
Coalescence

ABSTRACT

In this paper are reviewed some recent progress on the understanding and simulation of aluminum alloy age hardening. The main phenomena governing the formation of precipitate microstructures in aluminum alloys are presented; they provide a qualitative understanding of the relationship between alloy chemistry, processing and final precipitate microstructure at the nanoscale. In a second part, we describe how modeling approaches are capable of predicting these microstructures, from simple models to more advanced ones. A particular emphasis is put on the limits of these models and the strategies that are being developed to overcome them. In a third part, the mechanisms for precipitation strengthening will be discussed, as well as the models available to quantify this strengthening. Finally, in the last part, we will give some general prospects for the main developing areas of research.

RÉSUMÉ

Dans cet article, nous examinons quelques progrès récents en matière de compréhension et de simulation du durcissement par revenu des alliages d'aluminium. Les principaux phénomènes régissant la formation des précipités dans des alliages d'aluminium sont présentés. Ils fournissent une compréhension qualitative de la relation entre la composition des alliages, le traitement thermique et la taille des précipités à l'échelle nanométrique. Dans une seconde partie, nous décrivons comment les approches de modélisation sont capables de prédire ces microstructures, des modèles simples aux modèles plus avancés. Un accent particulier est mis sur les limites de ces derniers et sur les stratégies développées pour les surmonter. Dans une troisième partie, les mécanismes de durcissement des précipitations seront abordés, ainsi que les modèles disponibles pour quantifier ce

E-mail address: christophe.sigli@constellium.com (C. Sigli).

https://doi.org/10.1016/j.crhy.2018.10.012

durcissement. Enfin, dans la dernière partie, nous donnerons quelques perspectives générales.

1. Introduction

The science of age hardening in aluminum alloys dates back to 1906, when Alfred Wilm discovered that, after quenching, a duralumin Al–Cu(–Mg–Mn) alloy would progressively harden at room temperature. It took approximately 30 years to explain that this hardening was caused by the formation of very small zones that could be detected by small-angle X-ray scattering (SAXS). These zones were named in 1939 "Guinier–Preston (GP) zones" in reference to the two researchers who simultaneously and independently unraveled by SAXS the mysterious strengthening origin of duralumin, which could not be visualized by any microscope at that time [1]. Since then, high-resolution transmission electron microscopy and atom probe tomography have allowed quantitative characterization of the microstructure of age-hardened aluminum alloys.

In 1919, Merica et al. [2] suggested that relevant phase diagrams would reveal which alloys were candidates for precipitation hardening and would provide both the solutionizing temperature and the range of temperature needed for the precipitation process. This prescription led to a "golden age" of phase diagram measurements, which were compiled in 1959 by H.W.L. Phillips for aluminum alloys [3]. After the pioneering work of Larry Kaufman in the late 1960s [4], and the availability of computers, measured phase diagrams and thermodynamic data were combined to numerically assessed multicomponent phase diagram and establish thermodynamic databases (CALPHAD approach). This approach has been proven to be industrially very useful to adjust the composition and associated heat treatment of aluminum alloys at high enough temperatures (roughly above 300–350 °C for aluminum alloys).

At low temperature, the microstructure evolution of an age-hardening alloy and the resulting hardening behavior is not only driven by thermodynamics, but is also strongly dependent on kinetics aspects. The objective of this paper is to present some recent progress that has been achieved on understanding the fundamental mechanisms involved in precipitation and strengthening of age-hardening aluminum alloys and to introduce some modeling tools widely used or currently developed to predict precipitation, yield stress, and strain hardening. The concepts will be illustrated by case studies on different families of aluminum alloys throughout the paper.

In a first part, a review of the main phenomena governing the formation of precipitate microstructures in aluminum alloys will be given, which will provide a qualitative understanding of the relationship between alloy chemistry, processing and final precipitate microstructure at the nanoscale. In a second part, we will describe how modeling approaches can predict these microstructures, from simple models to more advanced ones. A particular emphasis is put on the limits of these models and the strategies that are being developed to overcome them. In a third part, the mechanisms for precipitation strengthening will be discussed, as well as the models available to quantify this strengthening. Finally, in the last part, we will give some general prospects for the main developing areas of research.

2. Fundamental mechanisms

2.1. Precipitation sequence during aging of multicomponent alloys

The classical description of the precipitation reaction from a supersaturated solid solution in an alloy system uses the notion of "precipitation sequence". The principle is that, for a given composition, the phase diagram predicts a stable phase that represents the ultimate endpoint of the reaction. This stable phase being usually incoherent, its nucleation is energetically costly because of its high interfacial energy with the matrix. It is thus kinetically favorable to first nucleate metastable phases, which have a lower thermodynamic driving force, but a lower nucleation barrier because of a higher coherency with the matrix. The succession of these metastable phases, with the progressive loss of coherency, is often called "precipitation sequence". In aluminum alloys, this sequence is sometimes presented as being unique for a given alloy system/family.

It is now clear, however, that the word "sequence" is misleading in the sense that it implies a fixed succession of reactions. It is probably more accurate to imagine a possible phase space in which the system chooses a "precipitation trajectory" depending on the conditions: composition, temperature history, mechanical processing history,... This is particularly true in complex multicomponent alloys where the trajectories may choose to shortcut some of the metastable phases or seemingly jump from a precipitation sequence to another with minor changes concerning alloy composition or thermomechanical process.

For the Al–Cu–(Mg) system, the age-hardening alloy prototype example, the precipitation sequence is proposed to be:

$$\text{supersaturated solid solution} \rightarrow \text{GP zones} \rightarrow \theta'' \rightarrow \theta' \rightarrow \theta\ (Al_2Cu)$$

In this system, GP zones are discs in the {100} planes, the θ'' precipitates are coherent plates in the {100} planes where as θ' is semi-coherent and θ is incoherent with the aluminum solid solution. This alloy system is the basis of the 2xxx

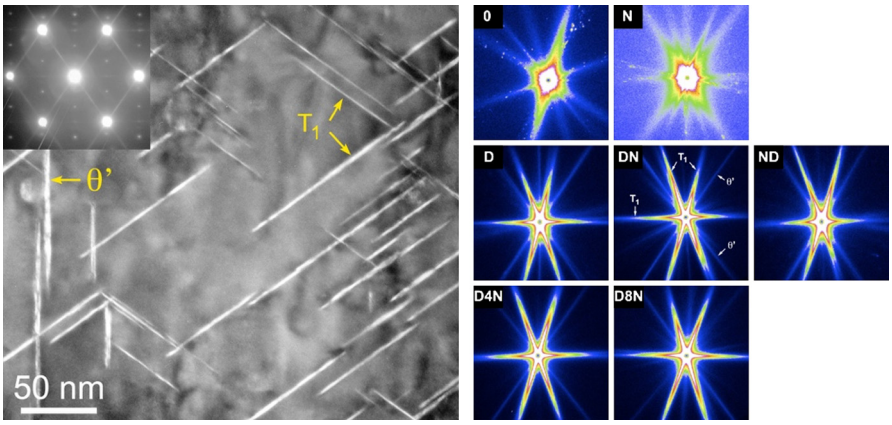

Fig. 1. (a) Microstructure of an Al–Cu–Li–Mg alloy after pre-deformation and aging at 155 °C showing the simultaneous presence of θ′ and T_1 precipitates within the grains. (b) Series of SAXS images after artificial aging, following different sequences of processing. O: Neither natural aging nor pre-strain; N denotes natural aging; D denotes deformation (D: 2%; D4 and D8: 4 and 8%). From [6].

family in aluminum alloys, which contains copper, magnesium, and optionally lithium as the major solute elements. This precipitation sequence applies when copper is the main solute addition. When the Mg content increases (e.g., the 2024 alloy), other phases may appear (GP zones, *S*′ which is based on Al_2CuMg and is semi-coherent, *S*, which is the incoherent Al_2CuMg precipitate). If Li is added, the achievable phase space is broadened by the addition of δ′ (Al_3Li) and other Li-rich phases. The combination of all these elements, as in the third generation of aerospace "Al–Li" alloys, which are basically composed of Al–Li–Cu–Mg plus other minor additions cannot be described by a single precipitation sequence. The potential phase space is now described by the phases of each individual binary alloy system as well as the relative ternary system phases, such as the T_1 (Al_2CuLi), T_2 (Al_6CuLi_3) or T_B ($Al_{15}Cu_8Li_2$) phases.

In such a complex space of potential phases, the actual precipitation trajectory will be very dependent on the actual composition and the thermo-mechanical processing. We will now give examples illustrating bifurcations in the trajectories.

Influence of the thermomechanical path Following the pioneering work of Gable et al. [5], Decreus and co-workers carried out a thorough study, on an Al–Cu–Li–Mg alloy, concerning the influence of the sequence between plastic deformation (or its absence) and natural aging on the subsequent precipitation kinetics and related strengthening during an aging at 155 °C [6]. In contrast to other aluminum alloy families, where natural aging is either favorable (7000 family, which contains zinc, magnesium, and optionally copper as major solute elements) or detrimental (6000 family, which contains magnesium, silicon, and optionally copper as major solute elements), in these alloys no significant effect of the clusters formed during natural aging was found on the artificial aging kinetics, and a combination of T_1 (Al_2CuLi) and θ′ (Al_2Cu) was always found (see Fig. 1a). However, their main finding was that if no pre-deformation were applied, the microstructure would be dominated by θ′, whereas as soon as pre-stretch was applied, T_1 would dominate θ′ inside the grains (Fig. 1b). Since both phases compete on the Cu content in the matrix, this shows that the pre-deformation helps the nucleation of the T_1 phase. This can be explained by the fact that this hexagonal phase may need the dissociation of dislocations to nucleate its basal plane on a stacking fault. This example nicely illustrates how one can trigger the bifurcation of a precipitation trajectory by a simple processing step such as a pre-deformation.

Influence of composition We take the example of two commercial aerospace Al–Cu–Li based alloys, AA2196 and AA2198. These two Al–Cu–Li–(Mg–Ag–Zr) alloys have essentially the same composition, with only Li varying (AA2198 has around 1 wt% Li, whereas AA2196 has between 1.4 and 2.1 wt% Li). After a typical industrial age-hardening heat treatment (16 h at 155 °C), the precipitates microstructure in AA2196 (high Li) consists in a mixture of δ′ (Al_3Li), θ′ (Al_2Cu), and T_1 (Al_2CuLi), as can be seen in Fig. 2a and 2b, which show transmission electron microscopy (TEM) dark-field images in the ⟨110⟩ viewing directions and highlights platelets in the {111} planes (T_1), platelets in the {001} planes (θ′) and spherical particles (δ′). Fig. 2c shows that, after the same heat treatments, the AA2198 (low Li) presents only T_1 Al_2CuLi precipitates. While this change in the precipitation sequence may not be entirely surprising, it is important because δ′ may have deleterious consequences on the long-term stability of the alloy, and it also profoundly influences the precipitation kinetics of the main strengthening phase, T_1. The δ′ precipitates were already present after natural aging; they mostly undergo some reversion and coarsening during aging and their presence seems to increase the incubation time for T_1 precipitation as well as their growth kinetics (Fig. 2d).

While this example showed the effect of a change in the main alloying element content, a further study based on similar alloys highlighted the strong influence of minor alloying elements on the precipitation sequence. Seven different alloys based on Al–3.5%Cu–0.9%Li with various amounts of minor alloying elements (Mg, Ag, Zn), alone or in combination, were tested. The most striking result was that the presence (0.35 wt%) or absence of Mg in this alloy drastically changed the

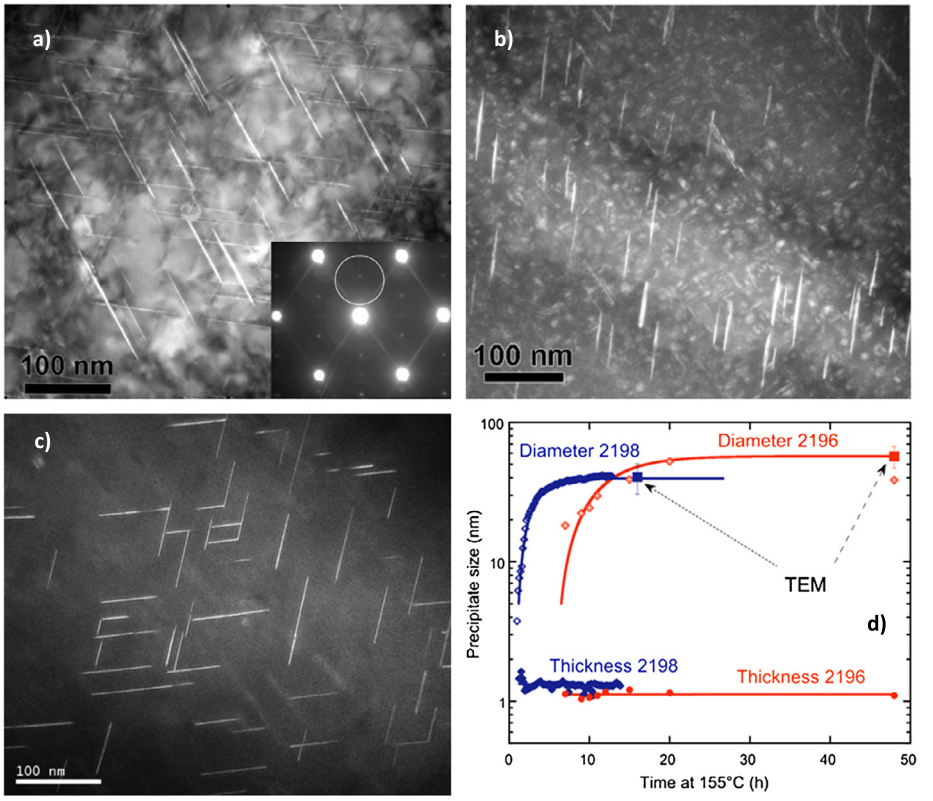

Fig. 2. (a) and (b) Dark-field TEM images of AA2196 alloy after aging viewed along a ⟨110⟩ matrix zone axis; (c) dark field TEM image of AA2198 alloy after aging viewed along a ⟨110⟩ matrix zone axis; (d) evolution of the thickness and diameter of precipitates during aging at 155 °C monitored by in-situ SAXS (from [7]).

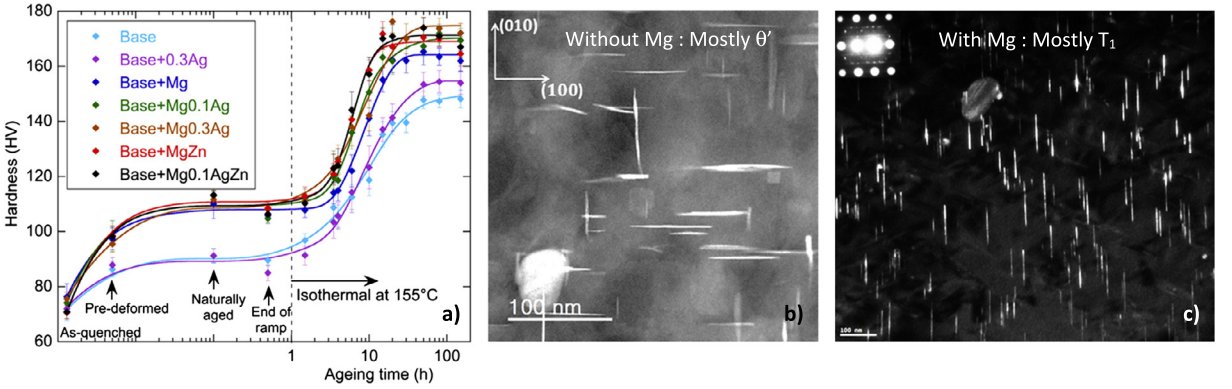

Fig. 3. (a) Evolution of hardness during an aging treatment at 155 °C for alloys with a base composition of Al–3.5 wt%Cu–0.9 wt%Li and different additions of Mg, Ag, and Zn; (b) dark-field TEM micrograph in ⟨100⟩ matrix direction of a Mg-free alloy and (c) dark-field TEM micrograph in ⟨112⟩ matrix direction of a Mg-containing alloy (from [8,9]).

precipitation kinetics of the T_1 precipitates (Fig. 3), even though this phase is not expected to contain a significant amount of Mg.

The effect of minor alloying elements on the precipitation sequence can have multiple origins. They may either directly act on the nucleation rate of this phase, for instance by lowering the stacking-fault energy, favoring the nucleation of the hexagonal phase. They may stabilize the phase by segregation and subsequent decrease of the interfacial energy. They may also have an indirect effect as it is believed to happen with Mg. A possible scenario is that Mg favors the formation of CuMg-rich objects at dislocations, which in turn enables the nucleation of T_1 at dislocations [9]. It seems that without Mg, it is rather θ′ that forms at dislocations; both phases compete for the same Cu content. This example shows some of the possible interactions involved when several alloying elements are present.

2.2. Precipitation–plasticity coupling

Precipitation processes in aluminum alloys can be profoundly changed by the interaction with crystal defects. Although all types of defects show interactions with precipitation (vacancies, dislocations, grain boundaries), the case of dislocations is particularly interesting and challenging to understand because of the dynamic nature of the interaction in the cases where dislocations are mobile, namely when precipitation occurs together with plastic deformation. From the point of view of applications, this coupling can occur in various situations, among which we can exemplify:

- decomposition of the supersaturated solid solution during plastic straining following a quench after solutionizing [10] (whose role is generally to decrease the level of quench-induced internal stresses),
- concurrent precipitation and strain during warm-forming processes such as age-forming, aiming at creating parts with complex shapes and low residual stress or improving formability as compared to room temperature [11,12],
- dynamic evolution of the microstructure during the service life of alloys subjected to plastic deformation (such as under fatigue) [13],
- microstructure evolution during joining processes involving plastic strain, such as Friction Stir Welding (FSW) [14,15],
- microstructure evolution during processes involving severe plastic deformation (SPD) [16].

Before giving examples of the variety of interactions that can be observed in these situations, it is useful to summarize some of the mechanisms that participate in the end-microstructure generation.

The first obvious possible effect of dislocations traveling through a precipitate-free supersaturated microstructure is to induce precipitate nucleation, at a rate larger than what would happen in the absence of these dislocations. Strain-induced nucleation is expected to be important in cases where plastic deformation is applied prior to any significant precipitation. It can be thought to be similar to the effect of static dislocations on precipitation, which is observed when artificial aging heat treatments are made on pre-deformed material [17].

The second set of possible effects is on the accelerated diffusion of solute atoms due to the dislocation movement, which results in an acceleration of all precipitation processes, from nucleation to growth and coarsening. The simple glide of dislocations through the crystal results in atomic movement, which may bring together some solute atoms and result in the formation of clusters. Since such dynamically formed clusters could subsequently be avoided by the next dislocations because of their hardening effect, a net formation of clusters could result from plastic deformation alone, without the need for long-range diffusion. This effect, sometimes called “ballistic”, has been invoked to explain abnormal strain hardening during straining at very low temperatures (4.2 K) of supersaturated solid solutions [10,18]. At more classical temperatures, long-range diffusion becomes, of course, dominant. Traveling dislocations may have a role in promoting the diffusion processes by pipe diffusion along their core. This effect can be amplified by the glide of dislocations that can act as solute collectors on the glide plane, and redistribute this solute by pipe diffusion to specific locations such as existing precipitates on which the dislocations are pinned. A further effect of dislocations on diffusion is the role of excess vacancies created by plastic deformation [19]. The net effect of plastic strain on vacancy concentration is a complex issue, which depends on the balance between the generation of excess vacancies by plastic strain, and their annihilation to defects (which include the traveling dislocations). This balance depends on many parameters such as strain rate, temperature, monotonic or periodic nature of straining, etc. However, when an excess concentration of vacancies is present, this accelerates naturally all diffusion processes and therefore all precipitation kinetics [12,13].

The third set of possible effects is somehow the reverse of the former. When precipitates are present in the microstructure during straining (which can apply to initial precipitates or to precipitates formed dynamically at earlier stages), they interact with the traveling dislocations. In the case where precipitates are sheared by dislocations, their geometry and free energy become modified by the shearing process. One dislocation alone results in an additional interface with the matrix (corresponding to a step width of one Burgers vector) and to a planar fault within the precipitates (stacking fault, anti-phase boundary…). Shearing by multiple dislocations, if occurring on the same shear plane, can result into a dramatic change, namely cutting the precipitate into two parts [20]. One can note that, for some precipitates such as Ω [21] or T_1 [22], multiple precipitate shearing is not favored, which prevents this type of catastrophic effect. If precipitates become repeatedly cut, this results in the increase of their surface-to-volume ratio, and they may eventually become unstable and dissolve back into the solid solution. Usually, such process requires relatively large strains, at least locally on a given glide plane.

We can now give a few examples of different cases with different dominating mechanisms. First, we can discuss the case of straining a precipitation hardening alloy (here, 7000 family Al–Zn–Mg–Cu alloys) at the artificial aging temperature, starting from an underaged microstructure, thus containing already some pre-existing precipitates. Practically, this case can address the age-forming process of aerospace alloys or the warm-forming process of high strength aluminum alloys for automotive applications. Experiments carried out using small-angle X-ray scattering give access to a very precise measurement of the evolution of the precipitate size with time and strain. In a first set of experiments dedicated to the study of age forming, measurements of precipitates were carried out in-situ during straining at 160 °C, with a relatively slow strain rate (between 10^{-5} and 10^{-3} s^{-1}) [12]. The experiment consisted in imposing a constant strain rate for a given level of strain (a few %) and then stopping deformation to evaluate the evolution of the microstructure due to the static effect of the introduced dislocations. Fig. 4 shows the evolution of strain, strain rate, stress, of the precipitate radius and its time derivative during two sets of experiments, one realized at slow strain rate and the other at a faster one. These experiments

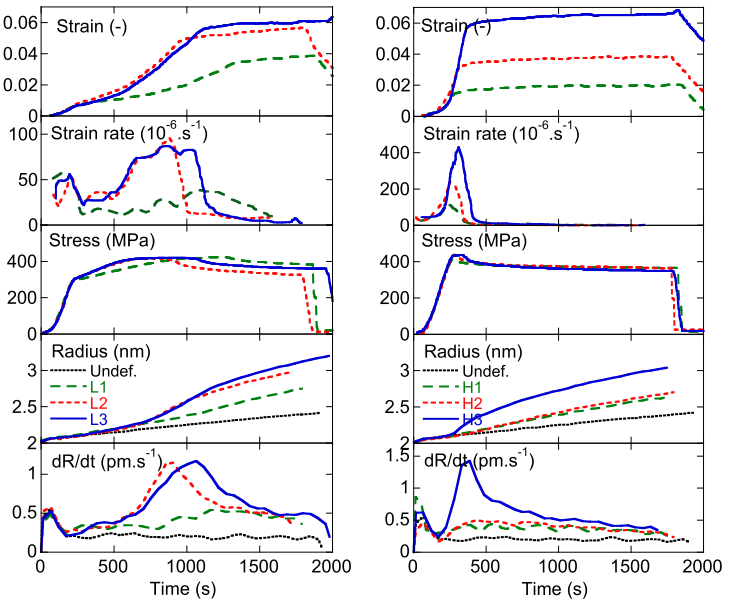

Fig. 4. Output from in-situ thermo-mechanical treatments performed on partially aged AA7449 alloy while monitoring the precipitate evolution with SAXS. Left: experiments at low strain rate; right: experiments at high strain rate (from [12]).

evidenced an acceleration of the size evolution due to plastic straining, which turned out to be proportional to the cumulative strain, but not the strain rate. These characteristics were found to be representative of excess vacancies being produced during straining and controlling the evolution of precipitates.

In the second example, devoted to the case of warm forming for potential applications in the automotive sector, the aim was to probe much larger strain rates such as what can be met in a forming operation. Therefore, in-situ experiments during straining could not be envisaged and, instead, experiments were carried out on samples with a variable cross-section, where the inherent heterogeneous distribution of strain allowed the evaluation of the precipitate microstructure after any level of imposed plastic strain [23]. These samples were scanned with small-angle X-ray scattering subsequently to plastic straining, to access the link between local strain, precipitate size and integrated intensity (proportional to the precipitate volume fraction). For two samples with different strain rates ($\sim 10^{-3}$ s^{-1} and ~ 2 s^{-1}), similarly to age-forming case, straining induced a precipitate size increase and a precipitate number density decrease probably due to an increased number of excess vacancies (Fig. 5). In this case, however, an increased strain rate resulted in a smaller dynamic precipitation effect, evidencing a different balance between generation and recovery of excess vacancies during plastic straining.

Similar results have been obtained during low-cycle fatigue at room temperature of an underaged 7000 family alloy, where dynamic precipitation during straining has been attributed to strain-induced excess vacancies [13].

We can now give an example of a case dominated by shearable precipitates dissolution. In the study of Chen and co-workers [24], an Al–Cu alloy was heat treated by a two-stage schedule resulting in a bimodal precipitate distribution comprising shearable GP zones as well as non-shearable θ′ precipitates. Monotonic straining of these samples resulted in an almost complete dissolution of the GP, probably due to the fact that GP zones are one atomic plane in thickness and particularly sensitive to dislocation cutting. Interestingly, the dissolution of these GP zones resulted in an increased level of solid solution during the tensile test; this improved the alloy strain hardening and consequently its ductility.

2.3. Heterogeneities after welding

Friction stir welding (FSW) is a solid-state joining process that has now been shown to be well adapted to many age-hardening aluminum alloys [25]. The process involves both a large amount of strain as well as a temperature exploration close to, but below the melting temperature. The combination of strain and heat leads to a highly inhomogeneous microstructure ranging from an unaffected base material (BM) to a heat-affected zone (HAZ), a thermo-mechanically affected zone (TMAZ) and a central zone often called nugget, where heat and deformation lead to the recrystallization of the material.

We have already discussed the interactions between precipitation, on the one hand, and heat or deformation, on the other hand. FSW of age-hardening alloy is a nice demonstration of the combination of these effects. We will take the example of an aerospace AA2050 Al–Cu–Li alloy that is strengthened, as we have already shown, by the formation of Al_2CuLi (T_1) precipitates as thin platelets in the {111} planes of aluminum. From an engineering point of view, one would like to have a precipitate microstructure as homogeneous as possible.

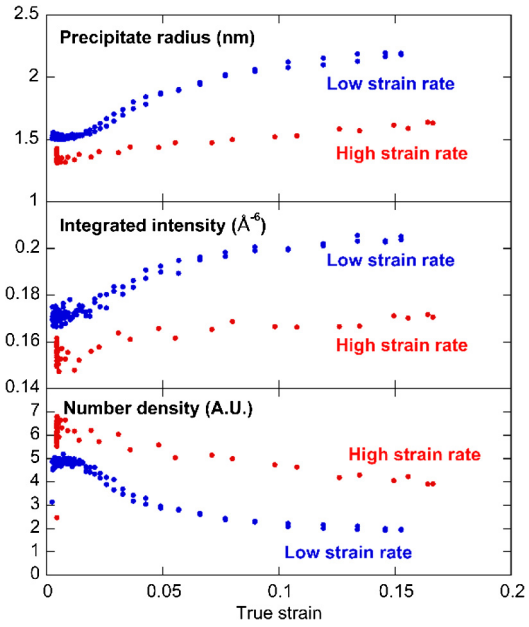

Fig. 5. Evolution of the precipitates Guinier radius, the associated integrated intensity and the resulting number density of precipitates with plastic strain for an underaged AA7068 alloy deformed at fast and low strain rate (from [23]).

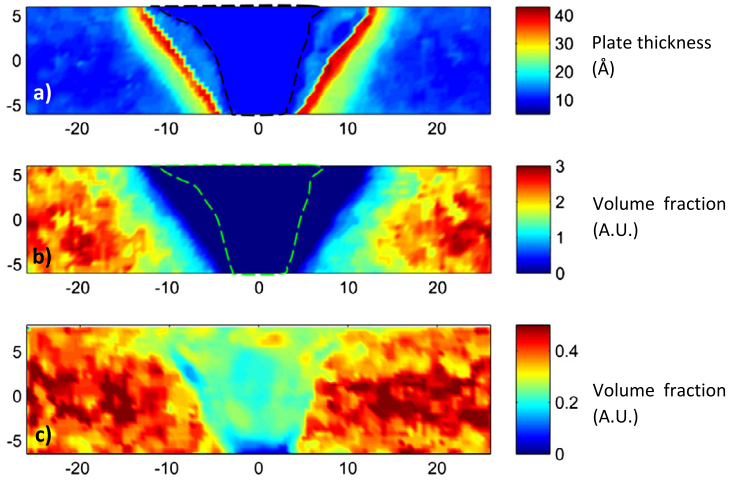

Fig. 6. Microstructure maps realized in cross-sections of friction stir welds of AA2050 alloy. (a) Map of precipitate thickness in a T8W weld (scale in Å); (b) map of precipitate volume fraction in the same T8W weld (arbitrary unit); (c) map of precipitate volume fraction in a T3WT8 weld (arbitrary unit) (from [26,27]).

There are (at least) two possible scenarios. Either the sheets are welded in the peak-aged state (T8), or they are welded before precipitation (in the naturally aged, T3 state) and are then aged. We will use T8W for the alloy welded in T8 state, and T3WT8 for the alloy welded in T3 state followed by a T8 heat treatment.

Fig. 6a and b show cross-sectional SAXS mappings of the precipitate thickness and fraction, respectively, for the T8W conditions. Since it was welded in the T8 condition, the base material (outermost regions) presents a homogeneous precipitation of Al_2CuLi (T_1) with a thickness of about 1 nm. Closer to the center, the T_1 volume fraction decreases, while their thickness increases, up to a point where T_1 disappears. This can be attributed to the local temperature evolution alone. This is confirmed by the dashed line in Fig. 6a and b, which is an outline of the recrystallized weld nugget.

It seems reasonable to assume that a more homogeneous precipitation state would be obtained for the T3WT8 scenario. The fraction of platelets precipitates is now shown in Fig. 6c. The transition from the homogeneous base material to a lower fraction central part is now more abrupt, and the fraction does not go to 0, confirming that the microstructure is indeed a bit more homogeneous. The central part is still very different from the base material, however. Also, the softer central part is now essentially composed by the recrystallized weld nugget. TEM shows that the platelets precipitates in the nugget are actually essentially θ' rather than T_1.

This spatial distribution of phases can be understood with previous sections. On a pre-existing T8 microstructure, temperature elevation above the solvus of T_1 explains its dissolution at the center. Farther from the center, where the temperature is between the aging temperature and the solvus temperature, the precipitates coarsened and the volume fraction decreased.

For the T3WT8 weld, the welding process had no influence in the BM, HAZ and TMAZ, because it left the material in a pre-deformed state that is favorable to the precipitation of T_1. In the weld nugget, however, the recrystallization occurring during welding has suppressed the dislocations, necessary for the nucleation of the T_1 phase, thus favoring θ' and leading to a lower strength after the normal T8 aging. A longer aging, or an introduction of new dislocations by rolling after welding, is actually shown to virtually suppress the hardness dip inside the nugget [27].

3. Towards quantitative predictions of microstructure and properties

Classical Nucleation and Growth Theories (CNGTs) are widely used for predicting precipitate size distribution evolutions. CNGTs are based on the modeling of the nucleation rate and the growth rate of a precipitate population. In the following, the nucleation and growth rate equations will be derived for the simple case of spherical precipitates.

Nucleation The nucleation rate $\mathrm{d}N/\mathrm{d}t$ gives the flux of precipitates reaching the critical size r^*, above which they are stable and grow:

$$\frac{\mathrm{d}N}{\mathrm{d}t} = N_0 Z \beta(r^*) \exp\left[-\frac{\Delta G^*}{k_B T}\right] I(t) \tag{1}$$

where N_0 is the nucleation site number density, Z is the Zeldovich factor, $\beta(r^*)$ is the absorption rate at the critical size, ΔG^* is the energy barrier for nucleation, k_B is the Boltzmann constant, T is the temperature and $I(t)$ is an incubation coefficient varying from 0 to 1 with $I(0) = 0$ and $I(\infty) = 1$.

The energy barrier ΔG^* and the Zeldovich factor are given, for spherical precipitates, by [28]:

$$\Delta G^* = \frac{16}{3}\pi \frac{\gamma^3}{(\Delta g_{ch} + \Delta g_{el})^2} \tag{2}$$

$$Z = \sqrt{\frac{\Delta G_P^*}{3\pi \times k_B \times T}} \times \frac{v_{at}^P}{\frac{4}{3}\pi \times r^{*3}} \tag{3}$$

where γ is the precipitate/matrix interfacial energy, Δg_{el} is the elastic misfit energy, Δg_{ch} is the driving force for precipitation and v_{at}^P is the atomic volume of the precipitate. For a precipitate containing N elements, the driving force is given by:

$$\Delta g_{ch} = \frac{1}{v_{at}^P} \sum_j^N X_j^P \left[\mu_j(X_j) - \mu_j\left(X_j^i\right)\right] \tag{4}$$

where X_j^P is the solute atom fraction of precipitates and $\mu_j(X_j)$ is the chemical potential of element j in the solid solution of concentration X_j (X_j^i is the solute concentration at equilibrium at the matrix/precipitate interface). Chemical potentials can be estimated from thermodynamic databases or from solubility products in the literature.

The absorption rate $\beta(r^*)$ has been derived by Russel, assuming that the limiting reaction rate is the reaction at the interface; it has been later generalized for multicomponent systems [29,30]:

$$\beta(r^*) = \frac{4\pi r^{*2}}{a^4} \left(\sum_j \frac{X_j^P}{D_j X_j}\right)^{-1} \tag{5}$$

where D_j is the diffusion coefficient of element j and a is the lattice parameter.

When the absorption rate is limited by long range diffusion, the following equation must be used:

$$\beta(r^*) = \frac{4\pi r^*}{v_{at}^M} \left(\sum_j \frac{X_j^P}{D_j X_j}\right)^{-1} \tag{6}$$

In aluminum alloys, the use of Eq. (6) is preferred (see, for example, refs. [31–33]).

The incubation coefficient $I(t)$ takes the form: $I(t) = 1 - \exp(-t/\tau)$ – see, for example, [34]. Note that this form is only valid for isothermal treatments and that the precise value of the incubation time depends on the initial short-range order of the solid solution.

Growth The growth equation of spherical precipitates is obtained *via* Fick's diffusion equation assuming a stationary solute concentration profile of element j and equilibrium at the matrix/precipitate interface:

$$\frac{\mathrm{d}r}{\mathrm{d}t} = \frac{D_j}{r}\frac{X_j^0 - X_j^i(r)}{\alpha X_j^P - X_j^i(r)} \tag{7}$$

where α is the ratio of atomic volumes of matrix and precipitates: $\alpha = v_{\mathrm{at}}^{\mathrm{M}}/v_{\mathrm{at}}^{P}$ and X_j^0 is the alloy composition of element j. The equilibrium solute concentrations $X_j^i(r)$ are given by the Gibbs–Thomson equation (see [35,36]):

$$\sum_j X_j^{\mathrm{P}}\left[\mu_j\left(X_j^i(r)\right) - \mu_j\left(X_j^i(\infty)\right)\right] = \frac{2\gamma v_{\mathrm{at}}^{\mathrm{P}}}{r} \tag{8}$$

Implementation Classical implementations of CNGTs are described by the so-called numerical model of Kampman and Wagner (KWN) [37]. They have been more recently implemented in the form of a "multi-class" open software ("Multi-Preci" in [38] and "PreciSo" in [29,30]). They are also proposed as accomplished commercial software packages ("Matcalc" in [39–41] and "TC-Prisma" in [42]).

At each time step, if the number of nuclei is larger than a critical value, a new class of precipitate is created with number density $N_i = \mathrm{d}N/\mathrm{d}t \times \Delta t$. Then all existing classes grow according to the solution to the non-linear system formed by Eqs. (7) and (8), leading to $R_i(t + \Delta t) = R_i(t) + \mathrm{d}r/\mathrm{d}t \times \Delta t$. Finally, the mass balance is performed to update the solute content of all solute species X_j via:

$$X_j = \frac{X_j^0 - \alpha X_j^{\mathrm{P}} f^{\mathrm{P}}}{1 - \alpha f^{\mathrm{P}}} \tag{9}$$

where f^{P} is the volume fraction of the precipitates: $f^{\mathrm{P}} = \sum_i 4/3\pi R_i^3 N_i$.

In order to get a smooth precipitate size distribution, it is sometimes necessary to add a new precipitate class between two existing ones or, possibly, to delete an existing class. Details on class management can be found in refs. [29,30].

The integration time step Δt is also optimized in such a way that it can increase exponentially (to correctly describe coarsening where precipitate mean radius varies as $\langle r\rangle \propto t^{1/3}$ and also decrease when time integration leads to unphysical results (e.g., negative solute concentrations).

Limits of CNGTs CNGTs are based on some important assumptions and contain limitations that hinder their application to simple systems:

- in its basic formulation, interfacial energy is isotropic and precipitates are *spherical*, which is far from reality in some systems (e.g., AlCuLi),
- *elastic misfit energy* or external stress effects are poorly described and often not explicitly accounted for, leading to an unphysical concept of "effective" interfacial energy,
- calculation of nucleation rate is based on monomer (single solute atom) diffusion,
- calculation of nucleation rate is based on Boltzmann statistics, which is valid for small super-saturations,
- diffusion fields around precipitates are supposed to be infinite (no impingement), which is not the case when the volume fraction of precipitates is more than a few percent,
- diffusion fields are supposed to be spherical, which does not hold for non-spherical precipitates or for precipitates growing on crystal defects (e.g., dislocations, grain boundaries).

In the next section, we will discuss recent attempts to overcome some of these difficulties.

3.1. Beyond classical nucleation and growth theories

3.1.1. Cluster Dynamics

Classical Nucleation Theory is closely related to Cluster Dynamics: many assumptions that are introduced in the classical nucleation rate equations are naturally embedded in the cluster dynamics formalism. While classical nucleation theory is generally coupled with a CALPHAD description of the solid solution free energy that generally ignores any short-range order, cluster dynamics allows a description of the short-range ordering within the solid solution, which ultimately gives birth to supercritical nuclei.

Assuming that the exchange between clusters/precipitates is limited to monomers (i.e. solute atoms solvated by aluminum atoms), the time evolution of the atomic fraction of a cluster containing n solute atoms (also called an n-mer), C_n, is given by the master equation:

$$\frac{\partial C_n}{\partial t} = C_{n-1}\beta_{n-1} - C_n(\alpha_n + \beta_n) + C_{n+1}\alpha_{n+1} \tag{10}$$

where β_n is the n-mer absorption rate (the same as the one used in Eq. (1); it is calculated using Eq. (6) for aluminum alloys), and α_n is the emission rate.

Equivalently, this master equation can be written in terms of exchange fluxes between clusters:

$$\frac{\partial C_n}{\partial t} = J_{n-1\to n} - J_{n\to n+1} \tag{11}$$

where the exchange flux between n-mer and $n+1$-mer is:

$$J_{n\to n+1} = C_n\beta_n - C_{n+1}\alpha_{n+1} \tag{12}$$

At equilibrium, all fluxes $J_{n\to n+1}$ must vanish and the emission rates can be deduced from the equilibrium cluster concentrations:

$$\alpha_{n+1} = \frac{\overline{C_n}}{\overline{C_{n+1}}}\beta_n \tag{13}$$

where $\overline{C_n}$ is the n-mer equilibrium fraction for a given temperature and concentration.

The equilibrium fraction, $\overline{C_n}$, is expressed as a function of the n-mer cluster free energy, G_n, and of the effective chemical potential μ:

$$\overline{C_n} = \exp\left(-\frac{G_n - n\mu}{kT}\right) \tag{14}$$

where

$$\mu = \mu_{\text{solute}} - \mu_{\text{solvant}} \tag{15}$$

As demonstrated by the pioneering work of Perini, Jacucci and Martin [43], based on accurate Monte Carlo calculations applied to cubic clusters containing less than twenty atoms, the usual description of the free energy as a simple sum of a volume term and a surface term (as used in classical nucleation and growth models) no longer holds for such cluster sizes. It was shown that the free energy of an n-mer is best fitted by the following expression:

$$G_n = an + bn^{2/3} + cn^{1/3} + d \tag{16}$$

The values of a (volume term), b (surface term proportional to the surface energy), c (corner term), and d are adjusted to reproduce the free energy values calculated by a Monte Carlo scheme of an n-mer *embedded in a pure solvent* at a given temperature. Applying the same calculation scheme to larger clusters (up to 400 solute atoms) over a large temperature range, Lépinoux [44] showed that this equation is still applicable provided that, at low temperatures, the size range on which the fitting procedure is applied is split into two parts (typically clusters containing less than 50 atoms and clusters containing more than 50 atoms). This approach has been tested on dilute alloys having an A1 FCC $\rightarrow$ $L1_2$ Al_3X ordering reaction during a heat treatment.

At the atomic scale, the energetics of these systems can be described by concentration-independent first- and second-nearest-neighbor effective pair interactions. It is reminded that an effective pair interaction between Al and X is defined as:

$$V_i = \epsilon^i_{\text{Al-X}} - \frac{\epsilon^i_{\text{X-X}} + \epsilon^i_{\text{Al-Al}}}{2} \tag{17}$$

where $\epsilon^i_{\text{Al-X}}$ refers to the ith-nearest-neighbor pair interaction between Al and X.

With this definition, a positive effective interaction reflects a repulsion between the solvent and the solute, whereas a negative value reflects an attraction between the solvent and the solute. The $L1_2$ phase can be described with a negative V_1 and a positive V_2. With this simple V_1-and-V_2 model, an n-mer will consist of its n solute atoms together with all the solvent atoms that are first and second nearest neighbor to its solute atoms. At low-enough temperatures, if V_1 is sufficiently negative (which will be the case in all the examples considered), the thermodynamic is entirely governed by V_2.

With such a pair interaction model, cluster dynamics approaches have been successfully applied to binary Al–Zr and Al–Sc alloys [33]. Comparison between Kinetic Monte Carlo and Cluster Dynamics indicates a reasonable agreement provided that the solute concentration is lower than a few tenths of atomic percent, as shown in Fig. 7.

An n-mer can have different enthalpy levels depending on its conformation. At 0 K, a cluster will be in its lowest enthalpy conformation (the most compact one) but, as temperature increases, higher enthalpy levels can be occupied as they are stabilized by entropy. The free energy of a cluster is therefore temperature dependent; it is also a function of the total solute content in the solid solution.

Indeed, when dealing with a very dilute alloy, the center of gravity of a given n-mer that is fluctuating in the solid solution can be placed on any lattice site; however, as the alloy concentration increases, more and more sites will be

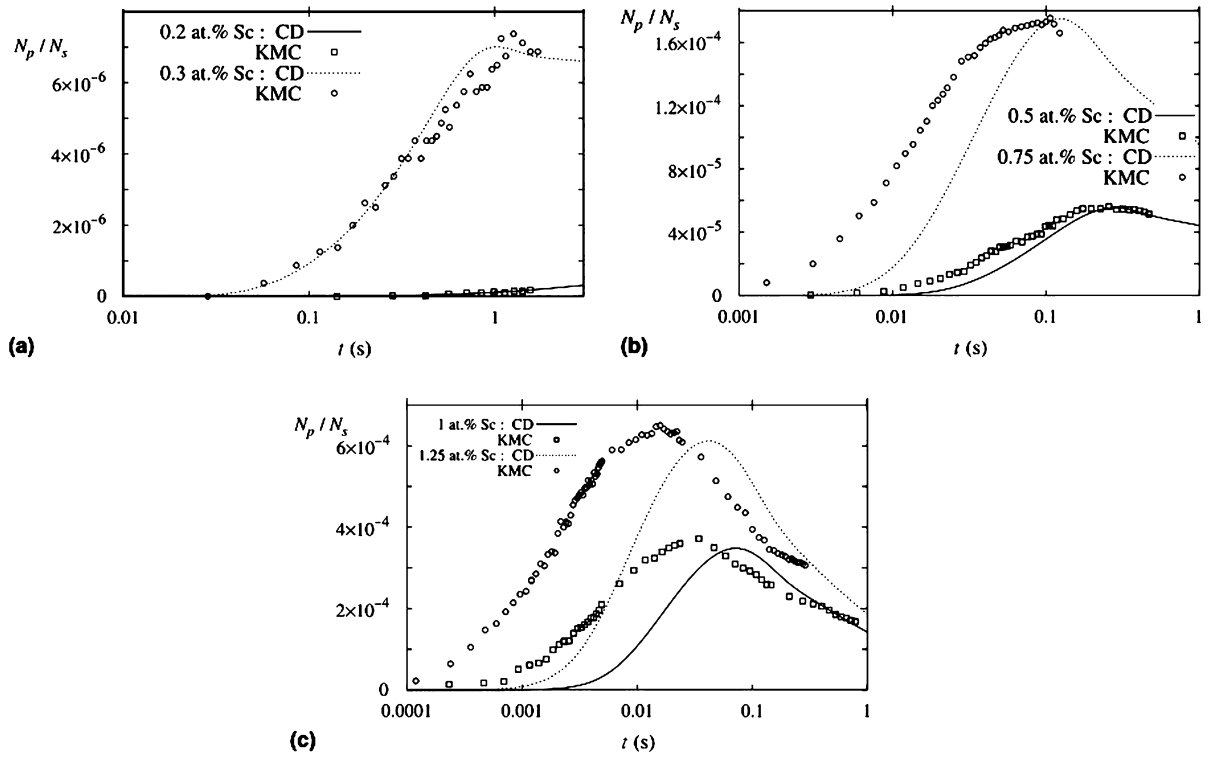

Fig. 7. Comparison between Cluster Dynamics and Kinetic Monte Carlo precipitation simulations in Al–Sc for Sc content ranging from 0.2 to 1.25 at% at a temperature of 450 °C (from [33]). The predicted density of Al_3Sc precipitates, N_p/N_s, is given as a function of time t.

occupied/excluded by other clusters, and the center of gravity of a given n-mer can only be placed on a limited fraction of sites [45–47]. This phenomenon is referred to as *cluster exclusion*; it is ignored in classical nucleation theory. A monomer that is surrounded by 12 first nearest neighbors and 6 second nearest neighbors has, for example, an exclusion volume of 19 atoms; a dimer has an exclusion volume of 32 atoms...

A simple approach to capture this effect is to assume that the free energy of an n-mer is the sum of its free energy in the very dilute case and of a corrective term taking into account the exclusion of the whole cluster population (details of the calculation are given in [45]). This correction is accurate enough provided the solute content is lower than approximately 1 at%.

When the solute concentration is higher than approximately 1 at%, it is not possible to have a simple additive correction term to the total free energy of an n-mer; the fact that each conformation of an n-mer has a different exclusion volume cannot be ignored anymore.

In general, the equilibrium atomic concentration of an n-mer, $C_{n,i}$, having an enthalpy h_i and a degeneracy $d_{n,i}$ can be written:

$$C_{n,i} = M_{n,i}\, d_{n,i}\, \mathrm{e}^{-(h_i - n\mu)/kT} \tag{18}$$

where $M_{n,i}$ is the fraction of the lattice site where the center of gravity of an n-mer in conformation i can be inserted.

For the monomer, i.e. a solute atom having only solvent atoms as first and second nearest neighbors, there is only one conformation, and we get the following equation:

$$C_1 = M_1 \mathrm{e}^{-(6V_2 - \mu)/kT} \tag{19}$$

For low-enough temperatures or dilute-enough alloys, the value of M_1 can be derived from a low-temperature expansion (LTE) [48,49]. If we retain enthalpy terms lower than $22V_2$ in the expression of C_1, we get the following expression for M_1:

$$M_1 = 1 - 19\mathrm{e}^{-\frac{(6V_2-1\mu)}{kT}} - 96\mathrm{e}^{-\frac{(10V_2-2\mu)}{kT}} - 663\mathrm{e}^{-\frac{(14V_2-3\mu)}{kT}} + 908\mathrm{e}^{-\frac{(12V_2-2\mu)}{kT}} \tag{20}$$

The first three negative terms represent exclusion from respectively monomers, dimers, and trimers (also named counter-terms in the LTE method). The fourth term is positive and represents a correction term linked to the exclusion of two monomers. As mentioned earlier, the LTE expressions can only be used for dilute-enough alloys (below a concentration of 0.5 at% with the LTE mentioned above). It must be remembered that M_1, which can be easily measured during KMC simulations, can be lower than 0.1 in very concentrated alloys [46,47].

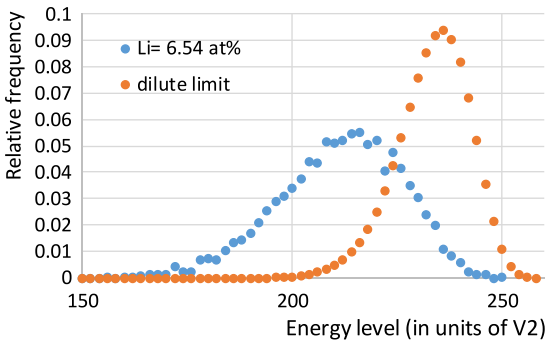

Fig. 8. Effect of the solid solution content on the energy occupancy frequencies of a 64-mer predicted by the Monte Carlo method at 200 °C.

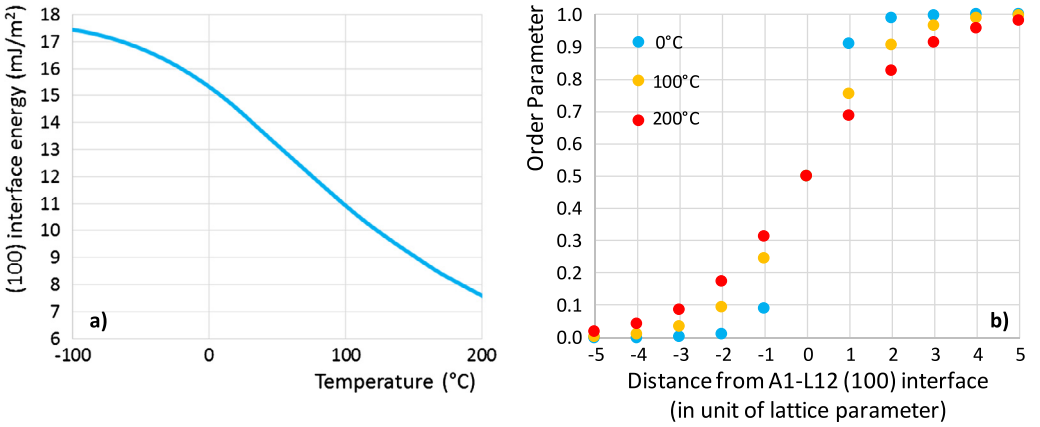

Fig. 9. (a) Dependence of the (100) A1–$L1_2$ interface energy with temperature for Al_3Li in Al. (b) Predicted variation of the diffuse interface width with temperature.

This exclusion effect is illustrated in Fig. 8, where we compare the energy levels occupied by a 64-mer at 200 °C in two cases: the 64-mer is immerged into pure aluminum or into a 6.54 at% Li solid solution. For this system, the value of the effective pair interaction V_2 is taken from Garland and Sanchez [50]. As can be observed, the enthalpy levels occupied by the 64-mer are significantly higher in the dilute case than the ones occupied in the 6.54 at% Li case. This is due to the fact that the higher energy levels occupy larger volumes and are less easy to insert in the solid solution due to the volume exclusion of the whole cluster population.

For alloys with a solute concentration higher than approximately 1 at%, it is necessary to tackle the precipitation modeling at an atomic scale using a Kinetic Monte Carlo approach, which is presented in &2.2.1.

Cluster Dynamics generally considers the adsorption or emission of a monomer from an *n*-mer. While this simple picture is often correct, it is not the only possible case. Indeed, in some alloys, it is necessary to account for the mobility of clusters of size larger than one solute atom to correctly reproduce KMC simulations [51,52] and, in such situations, the event-based Monte Carlo technique developed by Jourdan et al. is a promising approach [53].

3.1.2. Surface energy

The nucleation rate, and to a lesser extent the coarsening rate, are critically dependent on the precipitate/matrix interface energy. The latter is often assumed to be temperature independent and is tuned to reproduce the measured precipitate coarsening rate.

It must be emphasized, however, that the characteristics of the precipitate/matrix interface can strongly depend on temperature. An analysis performed by Asta [54] using V_1 and V_2 values from Garland and Sanchez [50] indicates that the interface energy of Al_3Li is reduced by a factor of two when the temperature is raised from 0 °C to 200 °C, as shown in Fig. 9a.

Although the effective pair interactions were chosen to be temperature independent, the resulting precipitate/matrix interface energy decreases significantly with temperature, which, in turn, will have a tremendous impact on the nucleation rate. This decrease is explained by an increasing roughening of the A1–$L1_2$ interface with temperature, which stabilizes the interface. The width of the diffuse interface has been calculated as a function of temperature for a (100) interface using an equilibrium Monte Carlo scheme, and the result is shown in Fig. 9b. As can be seen, this width reaches 10 unit cells (4 nm) for Al_3Li at 200 °C.

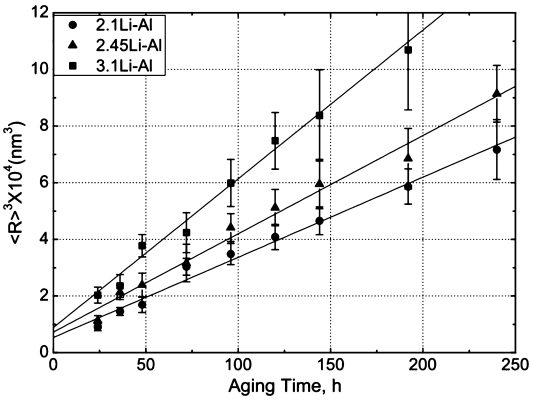

Fig. 10. Evolution of the cube radius with time during an aging at 225 °C for three binary alloys 2.1, 2.45, and 3.1 wt% Li (from [55]).

3.1.3. Overlap of diffusion fields

An important phenomenon that affects the coarsening rate of alloys with large solute contents is the overlap of diffusion fields; for binary Al–Li alloys, is it indeed observed [55] that the overall coarsening rate not only depends on temperature, but also depends on the density of precipitates (see Fig. 10). Glickman, Wang and co-workers [55,56] have proposed a multiplicative correction term, ϕ, on the growth/dissolution rate of a precipitate of radius R, which depends on a "diffusion screening" length, R_0, and on the precipitate fraction, f, and which reproduces experimental observations.

$$\phi = \left(1 + \frac{R}{R_0}\right) \quad \text{with } R_0 = \sqrt{\frac{\langle R^3 \rangle}{3\langle R \rangle f}} \tag{21}$$

3.1.4. Morphology of non-spherical precipitates

Efforts have been devoted to improving the CNGTs to account for more realistic shapes frequently observed in aluminum alloys (i.e. needles, plates). First of all, it is interesting to note that the physical origin of the precipitate morphology is not fully understood yet. The main factors influencing the shape of the precipitates are: (i) the anisotropy of the surface energy, (ii) the strain incompatibility of the precipitates and the matrix, and eventually (iii) the anisotropy of the elastic constants of the matrix and of the precipitates.

CNGTs do not claim to predict the actual shapes of precipitates, but rather to account for it in order to get more accurate nucleation and growth rates. Hillert [57] assumed steady-state growth and solved Laplace's diffusion equation around the tip of a plate and a needle. Simultaneously, Ham [58] proposed a slightly different expression for oblate and prolate ellipsoids. The general form of the growth equation for non-spherical precipitates is given by:

$$\frac{\mathrm{d}r}{\mathrm{d}t} = f \frac{D_j}{r} \frac{X_j^0 - X_j^i(r)}{\alpha X_j^{\mathrm{P}} - X_j^i(r)} \tag{22}$$

where f is a factor accounting for the non-spherical shape of the precipitates. Hillert's estimation has the advantage of proposing a simple form for this factor ($f = 1/2$ for a plate and $f = 3/4$ for a needle). Unfortunately, it does not degenerate into $f = 1$ for a sphere.

The Gibbs–Thomson equation is also modified due to the non-spherical shape of precipitates,

$$\sum_j X_j^{\mathrm{P}} \left[\mu_j\left(X_j^i(r)\right) - \mu_j\left(X_j^i(\infty)\right)\right] = \frac{2g\gamma v_{\mathrm{at}}^{\mathrm{P}}}{r k_{\mathrm{B}} T} \tag{23}$$

where g is another correction factor. In a recent contribution, based on a numerical 3D resolution of the diffusion equation, Holmedal et al. [59] proposed values for factors f and g, functions of the shape factor of ellipsoids. Similarly, Kozeschnik et al. [60] modified their evolution equations based on thermodynamic extremum principle and introduced cylindrical precipitates of various shape factors.

Bardel et al. [61] modeled the precipitation of needle-shaped β' of shape factor $\xi = l/r_{\mathrm{p}}$ (where l is the total precipitate length and r_{p} is the tip radius) in a 6061 alloy. They used the simplified factor $f = 3/4$ of Hillert and proposed a factor $g = 4\xi/(3\xi - 2)$ with a constant $\xi = 11$ value based on SANS experiments. They successfully compared the evolution of radius and volume fraction for various non-isothermal treatments.

More recently, Meyruey et al. [62] performed an extensive TEM investigation of β'' and β' precipitates in an Al–Mg–Si alloy with Si excess. They analyzed hundreds of precipitates and demonstrated a linear variation of the precipitate shape

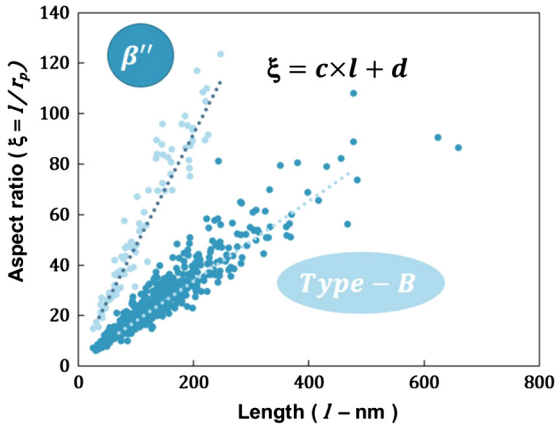

Fig. 11. Shape factors versus precipitate length in an Al–Mg–Si alloy with Si excess from TEM analysis [62].

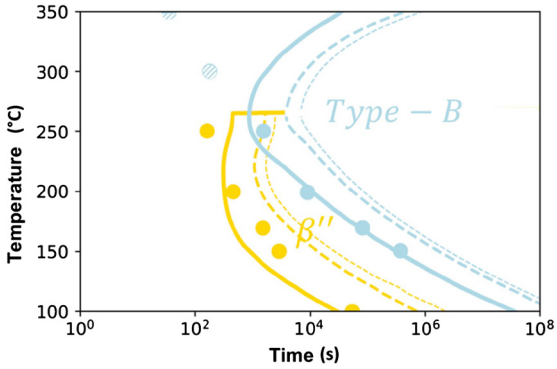

Fig. 12. TTT diagram of an Al–Mg–Si alloy with Si excess: comparison between experiments from [62] and KWN model with non-spherical precipitates (from [63]).

ratio with the length l (see Fig. 11). Two populations were identified as β'' ($\xi = 0.4\ \mathrm{nm}^{-1} l + 2.4$) and type-B precipitates ($\xi = 0.1\ \mathrm{nm}^{-1} l + 2$). From these shape factors and using the same f and g factors as Bardel et al. [61], they could successfully predict the TTT diagram of this alloy [63] (see Fig. 12).

3.2. Atomic-scale modeling

3.2.1. Rigid lattice

As already mentioned, for alloys with a solute concentration higher than 1 at%, it is advised to tackle the early stages of precipitation at the *atomistic scale* with a Kinetic Monte Carlo (KMC) approach in order to capture the strong exclusion effects on each n-mer; upscaling the model with cluster dynamics can be performed when, approximately, nucleation is finished; the exact moment when upscaling can be performed is beyond the scope of this paper.

In what follows, we give an example of a KMC simulation for a binary Al-4.75 at% Li alloy aged 2000 h at 85 °C. The thermodynamic description of the system is similar to that in Garland and Sanchez ($V_1 = -2V_2$), with a slightly higher value of V_2 in order to better reproduce the lithium solubility assessment of Noble and Bray ($V_2 = 1871$ J/mol instead of $V_2 = 1745$ J/mol). The kinetic Monte Carlo scheme used in this study assumes a direct exchange mechanism between the first nearest-neighbor atoms to simulate the diffusion process (Kawasaki dynamics). This approach is the simplest that can be implemented and needs very few input parameters: V_1, V_2, two parameters describing the diffusion coefficient of lithium in aluminum and the saddle-point energy barrier in pure aluminum. This scheme is much better than any mean field model to describe the early stages of precipitation; in general, however, it is advised to use a kinetic Monte Carlo scheme using a vacancy inside the Monte Carlo box, which allows the description of more complex diffusion paths.

The diffusion coefficient of Li is taken from Wen [64], with a pre-exponential factor of $1.55 \cdot 10^{-5}\ \mathrm{m^2\,s^{-1}}$ and an activation energy of 119.2 kJ/mol. The migration barrier energy of pure aluminum is 0.6 eV. The predictions of the model are presented in Fig. 13; they compare very well with SAXS measurements performed after 1000 h and 2000 h of aging at 85 °C.

For industrial applications, this model is coupled with an empirical Avrami-type precipitation model for the Al_2CuLi (T_1) phase that takes into account the effect of stretch on the precipitation kinetics: after an aging treatment of a given Al–Cu–Li alloy, the Li left in solid solution is calculated and used as an input for the Kinetic Monte Carlo model; it is then possible to

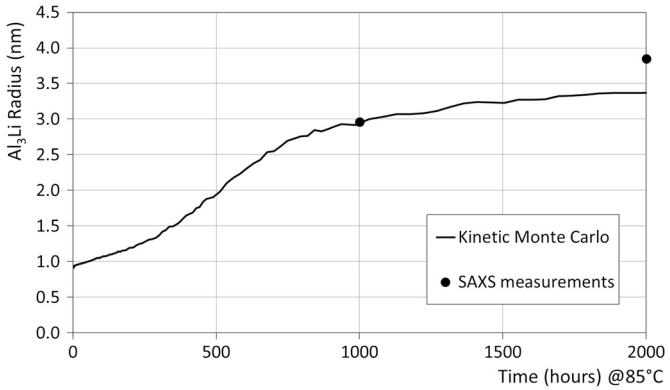

Fig. 13. Predicted evolution of the size of Al_3Li precipitates during long-term aging at 85 °C, as compared to SAXS.

predict the extent of precipitation of Al_3Li (δ') after long thermal exposition at 85 °C. This type of simulation is very useful because, in some cases, it is advisable to completely suppress the formation of AL_3Li during this exposition.

3.2.2. Relaxed lattice

As explained in the former section, atomistic simulations of precipitation help to overcome many limitations of mean field approaches (i.e. precipitate chemistry, morphology, diffusion fields, etc.). However, the influence of stress on precipitation and elastic misfit still remains a difficult problem with rigid lattice simulations (i.e. Monte Carlo).

Molecular Dynamics (MD) is the simplest way to relax the constraint of a rigid lattice. Its limited simulation time (of the order of a few ns with the fastest empirical potentials) makes it, however, impractical to use as a predictive tool for precipitation kinetics. To date, only a few contributions are devoted to the study of precipitation in aluminum alloys with relaxed lattice at the atomic scale. Among these, we can cite Hu et al. [65], who developed an interatomic potential and predicted surface energy, shape, and formation enthalpy of θ' precipitates in Al–Cu alloys.

Two strategies are currently under development.

(i) Acceleration of MD: many methods are proposed to save simulation time and concentrate on rare events driving the kinetics of the system (among which one can cite temperature-accelerated dynamics, parallel replica dynamics, hyperdynamics (see the review of Uberuaga, Perez and Voter [66] and the recent focused issue of JMR [67]). These methods are, however, currently limited to ps to ms, which is still too small for studying precipitation kinetics.
(ii) Coupling KMC with MD: KMC and MD are indeed two very complementary techniques: the first one is fast, but stresses are not accounted for, and the second one is just the opposite. Among these relaxed KMC methods, adaptive KMC [68], *k*-ART [69], and self-evolving atomistic KMC [70] are examples of recent developments, essentially applied to surface science and/or nuclear applications.

Application of such methods to aluminum alloys is still an open field that will certainly be tackled in the next few years.

3.3. Mechanical modeling of yield stress and hardening

The link between precipitate microstructures and the resulting yield strength is complex to understand quantitatively because it depends on numerous factors: first and foremost, of course, the type of interactions between precipitates and dislocations, sheared or bypassed. In the former case, it depends on whether the strength is controlled by the creation of an additional interface with the matrix, by the creation of a fault within the precipitate, by the elastic interaction between the precipitate and the dislocation, or by an elastic modulus difference between the two phases. However, additional parameters should be considered as well, namely the geometry of precipitates, their spatial distribution and orientation with respect to the glide planes, the size distribution of the precipitates. Of course, things become even more complex when several sets of obstacles are present, in which case the question of addition laws should be answered. Despite this complexity, considerable progress has been made in the last 10 years on this understanding, particularly because of the improved access to quantitative microstructure evaluations that can be used as a sound basis for comparing with models. Making a complete review of precipitation strengthening models and their application to aluminum alloys is beyond the scope of this article, so that we will give only a few examples of models compared with experiments in a few representative alloys.

Yield strength The yield strength of aluminum alloys is the result of four contributions added to the Peierls friction term σ_0: (i) the grain boundaries $\Delta\sigma_G = k_y/\sqrt{\phi}$, known as the Hall–Petch effect, where k_y is a constant and ϕ is the grain diameter; (ii) the solid-solution strengthening $\Delta\sigma_{ss} = k_j X_j^{2/3}$, where k_j is a constant and X_j is the solute content of element j; (iii) the forest term $\Delta\sigma_d = M\alpha\mu b\sqrt{\rho}$, where M is the Taylor factor, α is a constant of the order of 0.25–0.5, μ is the

shear modulus of aluminum, b is the Burgers vector and ρ is the dislocation density; (iv) the precipitate hardening effect $\Delta\sigma_{\mathrm{P}} = \sqrt{\Delta\sigma_{\mathrm{sh}}^2 + \Delta\sigma_{\mathrm{bp}}^2}$, where $\Delta\sigma_{\mathrm{sh}}$ and $\Delta\sigma_{\mathrm{bp}}$ are the contributions of sheared and bypassed precipitates, respectively. In a first approximation, these contributions can be added with a relatively simple addition law:

$$\sigma_y = \sigma_0 + R, \quad \text{with } R = \Delta\sigma_{\mathrm{G}} + \Delta\sigma_{\mathrm{ss}} + \sqrt{\Delta\sigma_{\mathrm{P}}^2 + \Delta\sigma_{\mathrm{d}}^2} \tag{24}$$

Based on areal glide simulations, more refined addition laws are available, taking into account the details of the relative obstacle strengths and number densities in the glide plane [71]. Depending on the precipitate shape (sphere, rods, plates), repartition in the shear plane, and distributions (monodisperse or polydisperse), many expressions of precipitate strengthening can be found in the literature. The most used approach is the mean field model developed by Friedel [72] and improved by Kocks et al. [73]. The main advantage of such approach is that the input parameters of the mechanical model are the output parameters of precipitation models or characterization, i.e. the precipitate size distribution and shapes.

On a polycrystalline material, the relation between the macroscopic stress increase $\Delta\sigma$ and the resolved shear stress τ is $\Delta\sigma = M\tau$. The stress increment due to precipitates is finally:

$$\Delta\sigma_{\mathrm{P}} = \frac{MF^{\mathrm{P}}}{bL} \tag{25}$$

where F^{P} is the force acting on the dislocation and L is the precipitate spacing. Depending on the interaction mechanism, F^{P} can have different expressions. For *bypassed* precipitates, $F^{\mathrm{P}} = 2\Gamma = 2\beta\mu b^2$ (Γ is the line tension, μ is the shear modulus of aluminum and β is a proportionality factor), leading to:

$$\Delta\sigma^{\mathrm{bp}} = \frac{2M\beta\mu b}{L} \tag{26}$$

For *sheared* precipitates, $F^{\mathrm{sh}} = k\mu b\bar{r}$ ($\bar{r}$ is the average intersect radius of precipitates within the shear plane; in the case of spheres, it is related to the precipitate radius R through $\bar{r} = R\pi/4$). If precipitates are sheared, the distance $L = L^{\mathrm{sh}}$ between obstacles that interact with the dislocation line now depends on the radius of curvature of the dislocation, which itself depends on the applied stress. Friedel [72] gave an estimation of L^{sh} ($L^{\mathrm{sh}} = \sqrt{2\Gamma/(F^{\mathrm{sh}}N_{\mathrm{a}})}$, where N_{a} is the surface density of obstacles in the shear plane), leading to:

$$\Delta\sigma^{\mathrm{sh}} = \frac{M}{b^2\sqrt{2\beta\mu}}\sqrt{{F^{\mathrm{sh}}}^3 N_{\mathrm{a}}} \tag{27}$$

The case of monodisperse spherical precipitates of radius r is a commonly used approximation, leading to:

$$\Delta\sigma^{\mathrm{bp}} = \frac{M\beta\mu b}{r}\sqrt{\frac{6f_v}{\pi}} \qquad \Delta\sigma^{\mathrm{sh}} = \frac{M\pi\mu k^{3/2}}{16}\sqrt{\frac{3f_v r}{\beta b}} \tag{28}$$

A relatively simple alloy system for the study of the shearing-to-bypassing transition is the Al–Zn–Mg–Cu system. Precipitates are relatively close to a spherical morphology; even though the η' precipitates have a plate morphology, their length remains at all times much smaller than their separation, so that they can be safely considered as isolated precipitates. Secondly, the evaluation of the strain hardening capacity as a function of heat treatment duration shows that the peak strength in this system coincides with the shearable-to-non-shearable transition [74]. Namely, as soon as peak hardness is passed, strain hardening dramatically increases at small strains as the result of the storage of geometrically necessary dislocations around non-shearable precipitates. In this case, the application of the above-mentioned models to shearable precipitates below the transition radius of 3.3 nm and for non-shearable precipitates above this radius yields an excellent agreement with microstructure data (size and volume fraction) from SAXS, as shown in Fig. 14. Only at peak strength is the model prediction higher than experimental data because the existence of a precipitate size distribution was not taken into account in this particular case. However, models exist to include this effect as well [75]. One should note that the existence of a peak strength, predicted to coincide with the shearable to non-shearable transition of Eq. (28) can arise in situations where this transition does not happen, or only for much larger precipitate sizes. In fact, peak strength is controlled by the saturation of obstacle strength. While the theory described before predicts this saturation to occur at twice the line tension (and therefore when precipitates become non-shearable), saturation could well occur at lower obstacle forces in the shearing regime. It has been actually proposed that, in some 6000-family aluminum alloys, precipitates remained shearable beyond peak strength [76,77].

The advantage of the approach presented above is that more complex geometries of precipitate–dislocation interactions can be accounted for. If precipitates are rods of length l and radius r aligned in the ⟨100⟩ directions and the shear planes are the {111} planes (see Fig. 15), the precipitate yield strength increase is then:

$$\Delta\sigma^{\mathrm{bp}} = \frac{2M\beta\mu b}{r}\sqrt{\frac{6f_v}{\pi}} \qquad \Delta\sigma^{\mathrm{sh}} = 3^{1/8}M\mu k^{3/2}\sqrt{\frac{f_v r}{2\pi\beta b}} \tag{29}$$

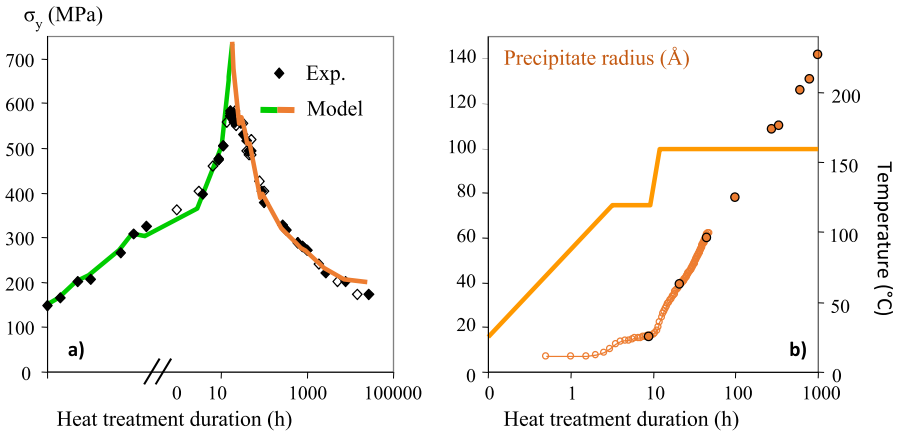

Fig. 14. (a) Evolution of yield strength as a function of aging at 160 °C in AA7449, compared with the predictions of a model for a shearing-to-bypassing transition, based on the quantitative characterization of precipitates by SAXS, as shown for the precipitate size in (b) (data taken from [74]).

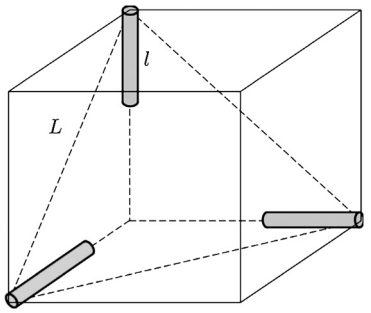

Fig. 15. Disposition of rods aligned in the ⟨100⟩ directions; the shear planes are the {111} planes (from [61]).

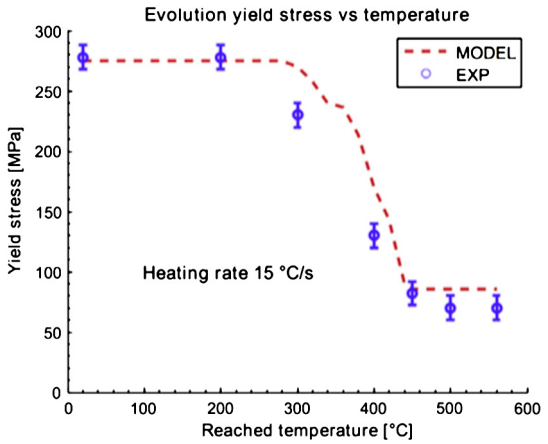

Fig. 16. Calculated and measured yield strength vs. the maximum temperature of the welding treatment (from [61]).

Bardel et al. adapted this approach to the case of β'' precipitates in a 6061 alloy accounting for the whole precipitate size distribution of rods (N_i is the number density of rods of length l_i and radius r_i) aligned in the ⟨100⟩ directions (see Fig. 16) [61]. It was then assumed that precipitates smaller than r_{i_c} were sheared, whereas larger ones were bypassed. The yield strength increase is then:

$$\Delta\sigma^{\mathrm{bp}} = \sqrt{2}M\beta\mu\sqrt{\sum_{i>i_c} N_i l_i} \qquad \Delta\sigma^{\mathrm{sh}} = 3^{\frac{1}{8}} M\mu k^{\frac{3}{2}} \sqrt{\frac{\sum_{i<i_c} N_i l_i}{2\beta b}} \left(\frac{\sum_{i<i_c} N_i l_i}{\sum_{i<i_c} N_i}\right)^{\frac{3}{2}} \tag{30}$$

The case of plate-like precipitates, however, requires a different modeling approach, since the precipitates cannot be considered as point obstacles when they interact with dislocations. In 2000-family alloys, most precipitates are indeed

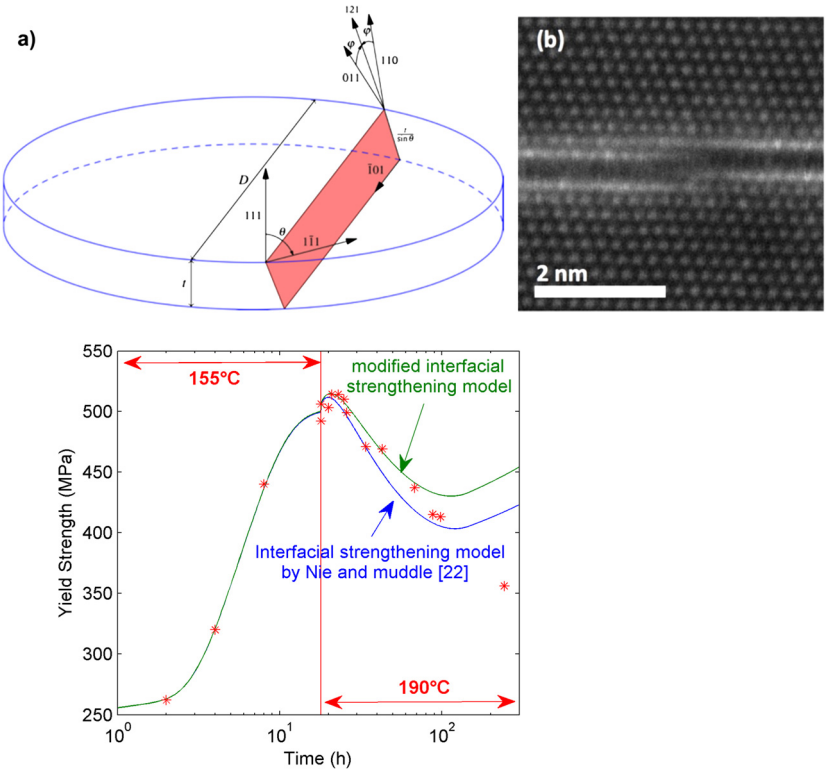

Fig. 17. (a) Schematic representation of the shearing mechanism of a T_1 precipitate by a dislocation; (b) corresponding high-resolution HAADF–STEM image in an AA2198-T8 alloy; (c) description of the yield strength evolution during aging at 155 °C based on this mechanism (from [80]).

plate-shaped. Nie and Muddle showed [78] that, under such geometry, the strengthening potential depends strongly on the habit plane, as well as on the aspect ratio of the precipitates. However, the details of the strengthening potential depend essentially again on the precipitate–dislocation interaction.

In the case of non-shearable precipitates (such as θ′ in Al–Cu), the strengthening problem becomes purely geometric. An important factor is the space remaining between the plates, which becomes the channels for dislocations to glide. Da Costa Teixeira et al. [79] made a quantitative assessment of the evolution of such spaces with aging and found a quantitative agreement with measured yield strengths in the Al–Cu system.

The situation becomes more complex when precipitates are shearable, which is the case for T_1 precipitates in Al–Cu–Li alloys [22]. This system is interesting because the peak strength does not coincide with the shearable-to-non-shearable transition. A relatively simple description of the strengthening in this case can be made by considering the energetic cost of shearing, namely the creation of a step at the precipitate/matrix interface, as well as the creation of a stacking fault within the precipitate (see Fig. 17). A model has been developed to describe the strengthening by such precipitates [80], refining a model first developed by Nie and Muddle [81], and based on Friedel statistics for the obstacle/dislocations interactions. This model is capable of describing precisely a wide range of microstructure/strength relationships where the precipitate characteristics have been varied independently, namely their thickness, diameter, number density, and volume fraction. According to this model, the maximum strength is obtained in this alloy for a maximum volume fraction of precipitates with a one-unit cell thickness, thereby requiring the highest amount of step formation during the shearing of these obstacles by dislocations. When precipitate thickening occurs (heat treatment at 190 °C in Fig. 17c), the strength is rapidly observed to decrease.

Strain hardening is also an important feature of aluminum alloys for manufacturing and/or optimization of final properties. It is the result of an isotropic component R due to the interaction between dislocations–defects interactions and one (or more) kinematic contribution(s) X due to the piling-up of dislocations on defects (e.g., grain boundaries, precipitates). These contributions can be introduced into an elastoplastic framework, where the stress σ is related to the plastic strain ϵ_p and the total strain ϵ through $\sigma = E(\epsilon - \epsilon_p)$, where E is the Young modulus. A yield function f delimiting the elastic domain is introduced:

$$f(\sigma, X, R) = |\sigma - X| - (\sigma_0 + R) \tag{31}$$

In the elastic domain ($f < 0$) and during plastic flow, $f = 0$. The normality rule provides the rate and direction of the plastic flow:

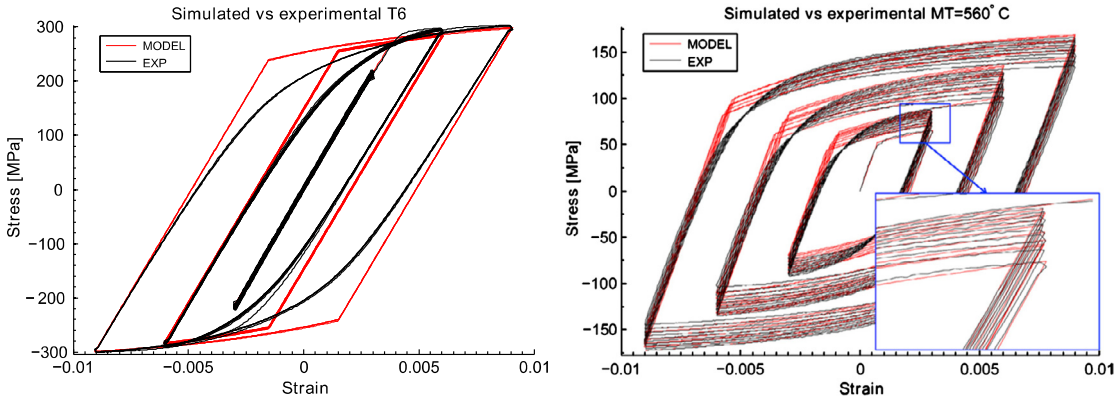

Fig. 18. Comparison between experimental and simulated cyclic deformation after two extreme thermal treatments on an AA6061 alloy: T6 and T6+heating at 560 °C (from [86]).

$$\dot{\epsilon}_p = \dot{\lambda}\frac{\partial f}{\partial \sigma} = \dot{\lambda}\,\mathrm{Sign}(\sigma - X) \tag{32}$$

where $\dot{\lambda}$ is the plastic multiplier, also defined as the norm of the plastic strain rate or the cumulative plastic strain rate $\dot{\lambda} = |\dot{\epsilon}_p| = \dot{p}$. It is determined by the consistency condition $f = 0$ during the flow, combined with Eqs. (31) and (32).

Isotropic hardening can be described by the classical Kocks–Mecking–Estrin (KME) [82,83] framework. It is based on a constitutive equation describing the evolution of the dislocation density ρ with strain:

$$\frac{\partial \rho}{\partial p} = (k_1\sqrt{\rho} - k_2\rho) \tag{33}$$

where k_1 and k_2 are constants describing work hardening and dynamic recovery.

Sinclair et al. [84] proposed an adaptation of the KME formalism in order to account for the contribution of grain boundary dislocations. They added an additional term in Eq. (33) to describe the efficiency of dislocations stored at the boundary with respect to forest hardening.

First introduced by Estrin [83] and later improved by Simar et al. [85], the contribution of Orowan loops to hardening was expressed as an additional term in Eq. (33). This version is also used by Fribourg et al. [74] for cyclic hardening in the presence of a distribution of precipitates.

Several authors accounted for the presence of precipitates in the estimation of the recovery parameter k_2 (see [83]). Simar et al. [85] stated that the presence of Orowan loops increases the stress field around precipitates, favoring cross-slip, thus leading to an amplification of dynamic recovery.

Kinematic hardening may be explained by dislocations pile-up on grain boundaries or precipitates. Based on the work of Sinclair et al. on grain boundary kinematic hardening [84], Bardel et al. [86] developed a specific framework for the kinematic hardening on precipitates and proposed a coupled equation:

$$X_{ppt} = \chi\frac{f_v^{bp}}{l^{bp}}n_{ppt} \quad \text{with } \frac{\partial n_{ppt}}{\partial \epsilon_p} = M\frac{l^{bp}}{b\sqrt{3}}\left(1 - \frac{n_{ppt}}{n^*_{ppt}\,\mathrm{Sign}(\dot{\epsilon}_p)}\right) \tag{34}$$

where χ is a constant, l^{bp} is the distance between bypassed precipitates, n^*_{ppt} is the maximum number of Orowan loops stored around precipitates.

Bardel et al. [86] accounted for isotropic and kinematic hardening and predicted the cyclic behavior of a 6061 alloy after various non-isothermal heat treatments. The precipitation model provides input parameters to the yield stress and hardening models. Fig. 18 compares the cyclic behavior of two samples at two different states: T6 (fully precipitated) and T6+heating at 560 °C (fully dissolved). The model is able to reproduce both yield stress and kinematic/isotropic hardening.

4. Perspectives

4.1. Combinatorial approaches

The number of parameters to be optimized in the design of a new alloy is very large. In typical age-hardening aluminum alloys, the number of solute species involved in the hardening precipitates lies between three and five (Al–Mg–Si–Cu, Al–Zn–Mg–Cu, Al–Cu–Li–Mg–Ag–Zn). New prospects for the development of high-temperature aluminum alloys also involve designing solute combinations with different diffusivities that could be activated at different temperatures. In addition to the complexity of adjusting the composition of a new alloy, the processing parameters to be adjusted are also numerous:

homogenization and solution treatment conditions, quenching rate, degree of pre-deformation, duration of natural aging, temperature (possibly multi-step) of the aging treatments. Thus, when modeling alone cannot provide a self-standing optimization of all these parameters, experimental approaches must work on the efficiency of the exploration of the alloy design space. Currently, combinatorial approaches are rapidly developing to answer this need. Although these approaches can encompass many different strategies (for a review, see in the same volume the paper dedicated to combinatorial approaches [87]), a particularly useful approach consists in fabricating materials with compositional gradient and/or materials with gradients of processing parameters (e.g., strain) and subsequently evaluate by a spatially resolved experimental technique (e.g., X-ray diffraction) the microstructure that develops in the different locations of these gradient materials. These approaches have been recently applied to the understanding of the effect of deformation and solute content on the clustering and precipitation kinetics in Al–Cu–Li alloys [88,89].

4.2. Modeling: DFT, KMC, and upscaling

The binary alloy atomistic energy description introduced in the previous sections is relatively simple. It consists of first- and second-nearest-neighbor effective pair interactions. With the progress of density functional theory (DFT) electronic structure calculations in speed and accuracy, it is possible to extract these effective interactions from DFT, allowing an exploration of the whole periodic table. Two approaches have gained interest to perform this task: the cluster expansion method, which has been recently used together with KMC to simulate GPI and GPII zones formation in an Al-2 at% Cu alloy [90] and, more recently, the neural network potential method used to investigate early stages of precipitation in Al–Mg–Si alloys [91,92]. DFT calculations are performed at 0 K, but it must be kept in mind that, in most instances, the phonon contribution to free energy needs to be calculated in order to reach the accuracy needed to reproduce a phase diagram. To perform these calculations, it is now possible to use good-quality Open Source Packages such as Quantum Espresso for DFT calculations and ATAT to extract a thermodynamic description from DFT results.

The maximum precipitate size or coarsening time that can be simulated by Kinetic Monte Carlo increase with the size of the Monte Carlo box. On the other hand, the simulation time dramatically increases with the box size and an upscaling of the simulation is needed beyond a certain time.

The above-mentioned tools allow an exploration of the whole periodic table for the identification of new promising ancillary or major additions to age-hardening aluminum alloys; these additions are further adjusted with a combinatorial experimental approach. Full-scale industrial casting and transformation is necessary to assess, for the most promising compositions, the complete set of properties required by a specific application such as corrosion, fatigue, formability, toughness, etc.

Acknowledgements

This paper summarizes the work of a number of former PhD and postdoctoral fellows who are gratefully acknowledged, and particularly D. Bardel, L. Couturier, B. Decreus, T. Dorin, G. Fribourg, E. Gumbman, B. Malard, and G. Meyruey. E. Clouet, F. Soisson and J.-C. Ehrström are also thanked for fruitful discussions. The staff of the BM02-D2AM beamline of ESRF is thanked for technical support when performing synchrotron experiments. A part of this work was performed within the framework of the Centre of Excellence of Multifunctional Architectured Materials “CEMAM” No. ANR-10-LABX-44-01.

References

[1] O. Hardouin Duparc, The Preston of the Guinier–Preston zones. Guinier, Metall. Mater. Trans., Phys. Metall. Mater. Sci. 41A (8) (2010) 1873–1882.
[2] D.R. Lide, K.H. Brown, A Century of Excellence in Measurements, Standards, and Technology, NIST, 2002.
[3] H.W.L. Phillips, Annotated Equilibrium Diagrams of Some Aluminium Alloy Systems, Monograph and Report Series, vol. 25, Institute of Metals, London, 1959.
[4] L. Kaufman, H. Bernstein, Computer Calculation of Phase Diagrams. With Special Reference to Refractory Metals, Academic Press, New York, 1970.
[5] B.M. Gable, A.W. Zhu, A.A. Csontos, E.A.J. Starke, The role of plastic deformation on the competitive microstructural evolution and mechanical properties of a novel Al–Cu–Li–X alloy, J. Light Met. 1 (14) (2001) 1–14.
[6] B. Decreus, A. Deschamps, F. de Geuser, C. Sigli, Influence of natural ageing and deformation on precipitation in an Al–Cu–Li alloy, Adv. Eng. Mater. 15 (11) (2013) 1082–1085.
[7] B. Decreus, A. Deschamps, F. De Geuser, P. Donnadieu, C. Sigli, M. Weyland, The influence of Cu/Li ratio on precipitation in Al–Cu–Li–x alloys, Acta Mater. 61 (2013) 2207–2218.
[8] E. Gumbmann, F. De Geuser, C. Sigli, A. Deschamps, Influence of Mg, Ag and Zn minor solute additions on the precipitation kinetics and strengthening of an Al–Cu–Li alloy, Acta Mater. 133 (2017) 172–185.
[9] E. Gumbmann, W. Lefebvre, F. De Geuser, C. Sigli, A. Deschamps, The effect of minor solute additions on the precipitation path of an AlCuLi alloy, Acta Mater. 115 (2016) 104–114.
[10] A. Deschamps, F. Bley, F. Livet, D. Fabregue, L. David, In-situ small-angle X-ray scattering study of dynamic precipitation in an Al–Zn–Mg–Cu alloy, Philos. Mag. 83 (6) (2003) 677–692.
[11] G. Fribourg, Y. Bréchet, J.-L. Chemin, A. Deschamps, Evolution of precipitate microstructure during creep of an AA7449 T7651 aluminum alloy, Metall. Mater. Trans. A 42 (2011) 3934–3940.
[12] A. Deschamps, G. Fribourg, Y. Brechet, J.-L. Chemin, C.R. Hutchinson, In situ evaluation of dynamic precipitation during plastic straining of an Al–Zn–Mg–Cu alloy, Acta Mater. 60 (5) (2012) 1905–1916.
[13] C.R. Hutchinson, F. de Geuser, Y. Chen, A. Deschamps, Quantitative measurements of dynamic precipitation during fatigue of an Al–Zn–Mg–(Cu) alloy using small-angle X-ray scattering, Acta Mater. 74 (2014) 96–109.

[14] C. Genevois, A. Deschamps, A. Denquin, B. Doisneau Cottignies, Quantitative investigation of precipitation and mechanical behaviour for AA2024 friction stir welds, Acta Mater. 53 (8) (2005) 2447–2458.
[15] C. Genevois, D. Fabrègue, A. Deschamps, W.J. Poole, On the coupling between precipitation and plastic deformation in relation with friction stir welding of AA2024 T3 aluminium alloy, Mater. Sci. Eng. A 441 (1–2) (2006) 39–48.
[16] A. Deschamps, F. De Geuser, Z. Horita, S. Lee, G. Renou, Precipitation kinetics in a severely plastically deformed 7075 aluminium alloy, Acta Mater. 66 (2014) 105–117.
[17] A. Deschamps, F. Livet, Y. Brechet, Influence of predeformation on ageing in an Al–Zn–Mg alloy – I. Microstructure evolution and mechanical properties, Acta Mater. 47 (1) (1999) 281–292.
[18] A. Deschamps, et al., Low-temperature dynamic precipitation in a supersaturated Al–Zn–Mg alloy and related strain hardening, Philos. Mag. A 79 (10) (1999) 2485–2504.
[19] M. Militzer, W. Sun, J. Jonas, Modelling the effect of deformation-induced vacancies on segregation and precipitation, Acta Metall. Mater. 42 (1) (1994) 133–141.
[20] C. Hutchinson, P. Loo, T. Bastow, A. Hill, J. Teixeira, Quantifying the strain-induced dissolution of precipitates in Al alloy microstructures using nuclear magnetic resonance, Acta Mater. 57 (19) (2009) 5645–5653.
[21] B.Q. Li, F.E. Wawner, Dislocation interaction with semicoherent precipitates (Omega phase) in deformed Al–Cu–Mg–Ag alloy, Acta Mater. 46 (15) (Sep. 1998) 5483–5490.
[22] A. Deschamps, B. Decreus, F. De Geuser, T. Dorin, M. Weyland, The influence of precipitation on plastic deformation of Al–Cu–Li alloys, Acta Mater. 61 (2013) 4010–4021.
[23] L. Couturier, A. Deschamps, F. De Geuser, F. Fazeli, W.J. Poole, An investigation of the strain dependence of dynamic precipitation in an Al–Zn–Mg–Cu alloy, Scr. Mater. 136 (2017) 120–123.
[24] Y. Chen, M. Weyland, C.R. Hutchinson, The effect of interrupted aging on the yield strength and uniform elongation of precipitation-hardened Al alloys, Acta Mater. 61 (15) (Sep. 2013) 5877–5894.
[25] A. Simar, Y. Bréchet, B. de Meester, A. Denquin, C. Gallais, T. Pardoen, Integrated modeling of friction stir welding of 6xxx series Al alloys: process, microstructure and properties, Prog. Mater. Sci. 57 (1) (2012) 95–183.
[26] F. De Geuser, B. Malard, A. Deschamps, Microstructure mapping of a friction stir welded AA2050 Al–Li–Cu in the T8 state, Philos. Mag. 94 (13) (2014) 1451–1462.
[27] B. Malard, F. De Geuser, A. Deschamps, Microstructure distribution in an AA2050 T34 friction stir weld and its evolution during post-welding heat treatment, Acta Mater. 101 (2015) 90–100.
[28] K.C. Russell, in: H.I. Aaronson (Ed.), Phase Transformations, American Society for Metals, 1968, pp. 219–268.
[29] M. Perez, M. Dumont, D. Acevedo, Implementation of the classical nucleation theory for precipitation, Acta Mater. 56 (2008) 2119–2132.
[30] M. Perez, M. Dumont, D. Acevedo-Reyes, Corrigendum to 'Implementation of classical nucleation and growth theories for precipitation', Acta Mater. 57 (4) (2009) 1318.
[31] E. Clouet, M. Nastar, A. Barbu, C. Sigli, G. Martin, Precipitation in Al–Zr–Sc alloys: a comparison between kinetic Monte Carlo, cluster dynamics and classical nucleation theory, in: Solid-Solid Phase Transformations in Inorganic Materials 2005, 2005.
[32] E. Clouet, M. Nastar, C. Sigli, Nucleation of Al_3Zr and Al_3Sc in aluminum alloys: from kinetic Monte Carlo simulations for classical theory, Phys. Rev. B 69 (2004) 064109.
[33] E. Clouet, A. Barbu, L. Laé, G. Martin, Precipitation kinetics of Al3Zr and Al3Sc in aluminum alloys modeled with cluster dynamics, Acta Mater. 53 (8) (May 2005) 2313–2325.
[34] P. Maugis, F. Soisson, L. Lae, Kinetics of precipitation: comparison between Monte Carlo simulations, cluster dynamics and the classical theories, Defect Diffus. Forum 237–240 (2005) 671–676.
[35] M. Perez, Gibbs–Thomson effect in phase transformations, Scr. Mater. 52 (2005) 709–712.
[36] Q. Du, M. Perez, W.J. Poole, M. Wells, Numerical integration of the Gibbs–Thomson equation for multicomponent systems, Scr. Mater. 66 (2012) 419–422.
[37] R. Wagner, R. Kampmann, P.W. Voorhees, Homogeneous second-phase precipitation, in: G. Kostorz (Ed.), Phase Transformations in Materials, Wiley-VCH Verlag GmbH & Co. KGaA, Weinheim, FRG, 2005, pp. 309–407.
[38] P. Maugis, M. Gouné, Kinetics of vanadium carbonitride precipitation in steel: a computer model, Acta Mater. 53 (2005) 3359–3367.
[39] E. Kozeschnik, J. Svoboda, P. Fratzl, F.D. Fischer, Modelling of kinetics in multi-component multi-phase systems with spherical precipitates: II: numerical solution and application, Mater. Sci. Eng. A 385 (1) (2004) 157–165.
[40] E. Kozeschnik, B. Buchmayr, MatCalc – A simulation tool for multicomponent thermodynamics, diffusion and phase transformation kinetics, in: Mathematical Modelling of Weld Phenomena, 2001, pp. 349–361.
[41] J. Svoboda, F.D. Fisher, P. Fratzl, E. Kozeschnik, Modelling of kinetics in multi-component multi-phase systems with spherical precipitates I: theory, Mater. Sci. Eng. A 385 (2004) 166–174.
[42] Q. Chen, K. Wu, G. Sterner, P. Mason, Modeling precipitation kinetics during heat treatment with CALPHAD-based tools, J. Mater. Eng. Perform. 23 (12) (2014) 4193–4196.
[43] A. Perini, G. Jacucci, G. Martin, Interfacial contribution to cluster free-energy, Surf. Sci. 144 (1) (1984) 53–66.
[44] J. Lepinoux, Interfacial reaction rates and free energy of cubic clusters, Philos. Mag. 85 (30) (2005) 3585–3621.
[45] J. Lepinoux, Contribution of matrix frustration to the free energy of cluster distributions in binary alloys, Philos. Mag. 86 (32) (2006) 5053–5082.
[46] J. Lepinoux, C. Sigli, On the effect of concentrated solid solutions on properties of clusters in a model binary alloy, Philos. Mag. 96 (10) (2016) 955–971.
[47] J. Lepinoux, C. Sigli, Multiscale modelling of precipitation in concentrated alloys: from atomistic Monte Carlo simulations to cluster dynamics I thermodynamics, Philos. Mag. 98 (1) (2018) 1–19.
[48] F. Ducastelle, Order and phase stability in alloys, in: F.R. De Boer, D.G. Pettifor (Eds.), Cohesion and Structure, vol. 3, North Holland, Amsterdam, The Netherlands, 1991.
[49] E. Clouet, Séparation de phase dans les alliages Al–Zr–Sc : du saut des atomes à la croissance de précipités ordonnés, PhD Thesis, École centrale, Paris, 2004.
[50] J. Garland, J. Sanchez, Cluster variation method calculation of the metastable aluminum–lithium phase diagram, in: Proc. Symposium on Kinetics of Ordering Transformations in Metals, TMS–AIME Annual Meeting, San Diego, CA, USA, March 4–5, 1992, pp. 207–216.
[51] K. Binder, D. Stauffer, Statistical theory of nucleation, condensation and coagulation, Adv. Phys. 25 (4) (1976) 343–396.
[52] T. Jourdan, F. Soisson, E. Clouet, A. Barbu, Influence of cluster mobility on Cu precipitation in α-Fe: a cluster dynamics modeling, Acta Mater. 58 (9) (May 2010) 3400–3405.
[53] T. Jourdan, J.-L. Bocquet, F. Soisson, Modeling homogeneous precipitation with an event-based Monte Carlo method: application to the case of Fe–Cu, Acta Mater. 58 (9) (2010) 3295–3302.
[54] M. Asta, Theoretical study of the thermodynamic properties of α–δ′ interphase boundaries in Al–Li, Acta Mater. 44 (10) (1996) 4131–4136.
[55] B.A. Pletcher, K.G. Wang, M.E. Glicksman, Experimental, computational and theoretical studies of δ′ phase coarsening in Al–Li alloys, Acta Mater. 60 (16) (2012) 5803–5817.

[56] K.G. Wang, M.E. Glicksman, K. Rajan, Length scales in phase coarsening: theory, simulation, and experiment, Comput. Mater. Sci. 34 (3) (2005) 235–253.
[57] M. Hillert, Role of interfacial energy during solid-state phase transformations, Jernkontorets Ann. 141 (1957) 757–789.
[58] F.S. Ham, Theory of diffusion-limited precipitation, J. Phys. Chem. Solids 6 (4) (1958) 335–351.
[59] B. Holmedal, E. Osmundsen, Q. Du, Precipitation of non-spherical particles in aluminum alloys part I: generalization of the Kampmann–Wagner numerical model, Metall. Mater. Trans. A 47 (2016) 581–588.
[60] E. Kozeschnik, J. Svoboda, F.D. Fischer, Shape factors in modeling of precipitation, Mater. Sci. Eng. A 441 (1) (2006) 68–72.
[61] D. Bardel, et al., Coupled precipitation and yield strength modelling for non-isothermal treatments of a 6061 aluminium alloy, Acta Mater. 62 (2014) 129–140.
[62] G. Meyruey, V. Massardier, W. Lefebvre, M. Perez, Over-ageing of an Al–Mg–Si alloy with silicon excess, Mater. Sci. Eng. A 730 (2018) 92–105.
[63] G. Meyruey, V. Massardier, M. Perez, Modelling the precipitation sequence of an Al–Mg–Si alloy with Si excess, 2018.
[64] C.J. Wen, W. Weppner, B.A. Boukamp, R.A. Huggins, Electrochemical investigation of solubility and chemical diffusion of lithium in aluminum, Metall. Trans. B 11 (1980) 131.
[65] S.Y. Hu, M.I. Baskes, M. Stan, L.Q. Chen, Atomistic calculations of interfacial energies, nucleus shape and size of theta′ precipitates in Al–Cu alloys, Acta Mater. 54 (18) (2006) 4699–4707.
[66] B.P. Uberuaga, D. Perez, A.F. Voter, Atomistic simulation methods for long-time dynamics in materials for nuclear energy systems, Los Alamos National Lab. (LANL), Los Alamos, NM, USA, LA-UR-18-25928, 2018.
[67] E. Martinez, D. Perez, V. Gavani, S. Kenny, Focus issue: advanced atomistic algorithms in materials science introduction, J. Mater. Res. 33 (7) (2018) 773–776.
[68] G. Henkelman, H. Jonsson, Long time scale kinetic Monte Carlo simulations without lattice approximation and predefined event table, J. Chem. Phys. 115 (21) (2001) 9657–9666.
[69] F. El-Mellouhi, N. Mousseau, L.J. Lewis, Kinetic activation–relaxation technique: an off-lattice self-learning kinetic Monte Carlo algorithm, Phys. Rev. B 78 (15) (2008) 153202.
[70] H. Xu, Y.N. Osetsky, R.E. Stoller, Simulating complex atomistic processes: on-the-fly kinetic Monte Carlo scheme with selective active volumes, Phys. Rev. B 84 (13) (2011) 132103.
[71] A. de Vaucorbeil, W.J. Poole, C.W. Sinclair, The superposition of strengthening contributions in engineering alloys, Mater. Sci. Eng., Struct. Mater.: Prop. Microstruct. Process. 582 (2013) 147–154.
[72] J. Friedel, Dislocations, Elsevier, 2013.
[73] B. Chalmers, J.W. Christian, U.F. Kocks, A.S. Argon, M.F. Ashby, Thermodynamics and Kinetics of Slip, Progress in Materials Science, vol. 19, Pergamon, Oxford, 1975.
[74] G. Fribourg, Y. Bréchet, A. Deschamps, A. Simar, Microstructure-based modelling of isotropic and kinematic strain hardening in a precipitation hardening aluminium alloy, Acta Mater. 59 (2011) 3621–3635.
[75] B. Holmedal, Strength contributions from precipitates, Philos. Mag. Lett. 95 (12) (2015) 594–601.
[76] A. Deschamps, S. Esmaeili, W.J. Poole, M. Militzer, Strain hardening rate in relation to microstructure in precipitation hardening materials, J. Phys. IV 10 (P6) (2000) 151–156.
[77] W.J. Poole, X. Wang, D.J. Lloyd, J.D. Embury, The shearable–non-shearable transition in Al–Mg–Si–Cu precipitation hardening alloys: implications on the distribution of slip, work hardening and fracture, Philos. Mag. 85 (2005) 3113–3135.
[78] J.F. Nie, B.C. Muddle, I.J. Polmear, The effect of precipitate shape and orientation on dispersion strengthening in high strength aluminium alloys, Mater. Sci. Forum 217–222 (1996) 1257–1262.
[79] J. Teixeira, D. Cram, L. Bourgeois, T. Bastow, A. Hill, C. Hutchinson, On the strengthening response of aluminum alloys containing shear-resistant plate-shaped precipitates, Acta Mater. 56 (20) (2008) 6109–6122.
[80] T. Dorin, A. Deschamps, F. De Geuser, C. Sigli, Quantification and modelling of the microstructure/strength relationship by tailoring the morphological parameters of the T1 phase in an Al–Cu–Li alloy, Acta Mater. 75 (2014) 134–146.
[81] J.F. Nie, B.C. Muddle, Microstructural design of high-strength aluminum alloys, J. Phase Equilib. 19 (6) (1998) 543.
[82] H. Mecking, U.F. Kocks, Kinetics of flow and strain-hardening, Acta Metall. 29 (11) (1981) 1865–1875.
[83] Y. Estrin, Dislocation density-related constitutive modeling, in: A.S. Krausz, K. Krausz (Eds.), Unified Constitutive Laws of Plastic Deformation, Academic Press, 1996.
[84] C.W. Sinclair, W.J. Poole, Y. Bréchet, A model for the grain size dependent work hardening of copper, Scr. Mater. 55 (8) (2006) 739–742.
[85] A. Simar, Y. Bréchet, B. de Meester, A. Denquin, T. Pardoen, Sequential modeling of local precipitation, strength and strain hardening in friction stir welds of an aluminum alloy 6005A-T6, Acta Mater. 55 (18) (2007) 6133–6143.
[86] D. Bardel, M. Perez, D. Nelias, S. Dancette, P. Chaudet, V. Massardier, Cyclic behaviour of a 6061 aluminium alloy: coupling precipitation and elastoplastic modelling, Acta Mater. 83 (2015) 256–258.
[87] A. Deschamps, F. Tancret, I.-E. Benrabah, F. De Geuser, H. Van Landeghem, Combinatorial approaches for the design of metallic alloys, C. R. Physique 19 (2018), https://doi.org/10.1016/j.crhy.2018.08.001 (in this issue).
[88] E. Gumbmann, F. De Geuser, A. Deschamps, W. Lefebvre, F. Robaut, C. Sigli, A combinatorial approach for studying the effect of Mg concentration on precipitation in an Al–Cu–Li alloy, Scr. Mater. 110 (2016) 44–47.
[89] R. Ivanov, A. Deschamps, F. De Geuser, High throughput evaluation of the effect of Mg concentration on natural ageing of Al–Cu–Li–(Mg) alloys, Scr. Mater. 150 (2018) 156–159.
[90] X. Zhang, M.H.F. Sluiter, Cluster expansions for thermodynamics and kinetics of multicomponent alloys, J. Phase Equilib. Diffus. 37 (1) (2016) 44–52.
[91] R. Kobayashi, D. Giofre, T. Junge, M. Ceriotti, W.A. Curtin, Neural network potential for Al–Mg–Si alloys, Phys. Rev. Mater. 1 (5) (2017) 053604.
[92] D. Giofre, T. Junge, W.A. Curtin, M. Ceriotti, Ab initio modelling of the early stages of precipitation in Al-6000 alloys, Acta Mater. 140 (2017) 240–249.